M. A. AWAN

TOWARDS MILLIMETER WAVE ALTIMETRY FOR UNMANNED AERIAL SYSTEMS

THE GRADUATE SCHOOL OF NATURAL AND APPLIED SCIENCES
OF
ATILIM UNIVERSITY

MAAZ ALI AWAN

A MASTER OF SCIENCE
THESIS
IN
THE DEPARTMENT OF ELECTRICAL AND ELECTRONICS ENGINEERING

SEPTEMBER 2024

ATILIM UNIVERSITY 2024

TOWARDS MILLIMETER WAVE ALTIMETRY FOR UNMANNED AERIAL SYSTEMS

A THESIS SUBMITTED TO
THE GRADUATE SCHOOL OF NATURAL AND APPLIED SCIENCES
OF
ATILIM UNIVERSITY

BY

MAAZ ALI AWAN

IN PARTIAL FULFILLMENT OF THE REQUIREMENTS
FOR
THE DEGREE OF MASTER OF SCIENCE
IN
THE DEPARTMENT OF ELECTRICAL AND ELECTRONICS ENGINEERING

SEPTEMBER 2024

Approval of the Graduate School of Natural and Applied Sciences, Atılım University.

_____

Prof. Dr. Ender KESKİNKILIÇ
Director

I certify that this report satisfies all the requirements as a thesis for the degree of **Master of Science in Electrical and Electronics Engineering, Atılım University**.

_____

Prof. Dr. Reşat Özgür DORUK
Head of Department

This is to certify that we have read the project TOWARDS MILLIMETER WAVE ALTIMETRY FOR UNMANNED AERIAL SYSTEMS submitted by MAAZ ALI AWAN and that in our opinion it is fully adequate, in scope and quality, as a thesis for the degree of Master of Science.

_____

Assoc. Prof. Dr. Yaser DALVEREN
Supervisor

Examining Committee Members:

Prof. Dr. Ali KARA
Electrical and Electronics Eng. Dept.
Gazi University _____

Prof. Dr. Reşat Özgür DORUK
Electrical and Electronics Eng. Dept.
Atılım University _____

Prof. Dr. Yaser DALVEREN
Electrical and Electronics Eng. Dept.
İzmir Bakırçay University _____

Date: *14th September 2024*

I hereby declare that all information in this document has been obtained and resented in accordance with academic rules and ethical conduct. I also declare that, as required by these rules and conduct, I have fully cited and referenced all material and results that are not original to this work.

Name, Last Name: Maaz Ali Awan

Signature:

ABSTRACT

TOWARDS MILLIMETER WAVE ALTIMETRY FOR UNMANNED AERIAL SYSTEMS

Awan, Maaz Ali

M.Sc., Department of Electrical & Electronics Engineering

Supervisor: Assoc. Prof. Dr. Yaser DALVEREN

September 2024, 64 pages

Accurate altitude data are crucial for the autonomous landing of UAS. Laser sensors, barometric altimeters, and GPS are limited by slow update rates, temperature sensitivity, and poor visibility. In commercial aviation, RAs are designed according to the MOPS. However, novel approaches are needed due to 5G networks interfering with the globally allocated RA band from 4.2–4.4 GHz. Contemporary mmWave automotive radars, with superior SWaP metrics, offer untapped potential for UAS altimetry. This study aims to derive waveform parameters of an automotive mmWave FMCW radar by adapting commercial aviation MOPS of RA for the UAS use case. The thesis proposes a methodology for maximizing performance metrics within the radar constraints of limited intermediate frequency IF BW and Tx power. Specifics of FMCW waveform design for the landing approach stage are presented. The study explores the potential of TDM-MIMO for improving the AoA resolution to augment situational awareness during autonomous landing. The study also characterizes variants of CFAR for terrain sensing. Lastly, it aims to address ambiguity arising from radial velocity due to the rapid descent of UAS in the landing phase and proposes potential remedial actions.

Keywords: mmWave, FMCW, RA, UAS, TDM-MIMO, CFAR

ÖZ

İNSANSIZ HAVA SİSTEMLERİ İÇİN MİLİMETRE DALGA ALTİMETRİSİNE DOĞRU

Awan, Maaz Ali
Yüksek Lisans, Elektrik ve Elektronik Mühendisliği Bölümü
Tez Yöneticisi: Doç. Dr. Yaser DALVEREN

Eylül 2024, 64 sayfa

İnsansız hava sistemlerinin otonom inişi için doğru irtifa verileri kritik öneme sahiptir. Lazer sensörleri, barometrik altimetreler ve Küresel Konumlama Sistemi, yavaş güncelleme hızları ve sıcaklık hassasiyeti nedeniyle sınırlıdır. Ticari havacılıkta radar altimetreleri minimum operasyonel performans standartlarına göre tasarlanır; ancak, 5G ağlarının 4.2–4.4 GHz aralığındaki radar bandına müdahalesi yeni yaklaşımlara ihtiyaç doğurmaktadır. Milimetre dalga otomotiv radarları, üstün boyut, ağırlık ve güç ölçütleriyle insansız hava sistemleri için kullanılmamış bir potansiyel sunmaktadır. Bu çalışma, ticari havacılıktaki radar altimetre performans standartlarını insansız hava sistemleri için uyarlayarak bir otomotiv milimetre dalga frekans modülasyonlu sürekli dalga radarının dalga formu parametrelerini türetmeyi amaçlamaktadır. Tez, ara frekans filtre bant genişliği ve iletim gücü radar kısıtlamaları içinde performans ölçütlerini en üst düzeye çıkarmak için bir metodoloji önermektedir. İniş aşaması için dalga formu tasarımının ayrıntıları sunulmuştur. Çalışma, otonom iniş sırasında durumsal farkındalığı artırmak için gelişmiş varış açısı çözünürlüğü sağlama potansiyeline sahip Zaman Bölmeli Çoğullama ile Çoklu Giriş Çoklu Çıkış yöntemini incelemektedir. Son olarak, insansız hava sistemlerinin iniş aşamasındaki radyal hız belirsizliğini ele almayı ve olası çözüm yolları önermeyi hedeflemektedir.

Anahtar Kelimeler: mmWave, FMCW, RA, UAS, TDM-MIMO, CFAR

DEDICATION

To my wife, parents, and children

ACKNOWLEDGMENTS

I want to express my deepest gratitude to Dr. Yaser DALVEREN for his invaluable supervision and unwavering support throughout this research journey.

I especially acknowledge Dr. Ali KARA for his inspiring discussions, immense support, and innovative ideas that helped shape this work. I am also profoundly thankful to Dr. Badar-ud-din AHMED for his exceptional mentorship and continuous encouragement.

I am profoundly indebted to my parents for their prayers, unconditional love, and constant belief in me. Finally, to my wife, whose sacrifices and steadfast support made this endeavor possible.

TABLE OF CONTENTS

LIST OF TABLES

LIST OF FIGURES

LIST OF SYMBOLS/ABBREVIATIONS

UAS	Unmanned Aerial System
AHRS	Attitude and Heading Reference System
GPS	Global Positioning System
PPS	Pulse Per Second
MSL	Mean Sea Level
AGL	Above Ground Level
LiDAR	Light Detection and Ranging
RA	Radar Altimeter
EM	Electromagnetic
FMCW	Frequency Modulated Continuous Wave
Tx	Transmit
Rx	Receive
LO	Local Oscillator
mmWave	Millimetre Wave
nm	Nanometre
RFCMOS	Radio Frequency Complementary Metal Oxide Semiconductor
MMIC	Monolithic Microwave Integrated Chip
MCU	Micro Controller Unit
HWA	Hardware Accelerator
DSP	Digital Signal Processor
RFFE	Radio Frequency Front End
ADAS	Advanced Driver Assistance Systems
HPBW	Half Power Beam Width
MOPS	Minimum Operational Performance Standards
AoA	Angle of Arrival
VTOL	Vertical Take-off and Landing
SWaP	Size, Weight, and Power

ADC	Analog to Digital Converter
CFAR	Constant False Alarm Rate
TDM-MIMO	Time-Division Multiplexing Multiple Input Multiple Output
ROD	Rate of Descent
PFA	Probability of False Alarm
BiCMOS	Bi-Polar Complementary Metal Oxide Semi-Conductor
SiGe	Silicon Germanium
5G	Fifth Generation Standard for Cellular Communication
nm	nanometre
GHz	Gigahertz
BW	Bandwidth
MHz	Mega Hertz
FSPL	Free Space Propagation Loss
SNR	Signal-to-Noise Ratio
IF	Intermediate Frequency
RCS	Radar Cross Section
3D	Three Dimensional
DL	Deep Learning
FFT	Fast Fourier Transform
TI	Texas Instruments
SDK	Software Development Kit
LoS	Line of sight
I/Q	In-phase and quadrature
LFM	Linear Frequency Modulated
RTOF	Round Trip Time of Flight
FOV	Field of View
NRCS	Normalized Radar Cross Section
RMS	Root Mean Squared
NF	Noise Figure

PCB	Printed Circuit Board
2D	Two Dimensional
PRI	Pulse Repetition Interval
LUT	Look Up Table
DFT	Discrete Fourier Transform
TOF	Time of Flight
PSD	Power Spectral Density
SIMO	Single Input Multiple Output
DC	Direct current
cm	Centimetre
ms	milliseconds
CFAR-CA	CFAR cell averaging
CFAR-CASO	CFAR cell averaging smallest of
CFAR-CAGO	CFAR cell averaging greatest of
BPM-MIMO	Binary phase modulation multiple input–multiple output
fpm	Feet Per Minute
TSC	Technology Service Corporation
APL	Applied Physics Laboratory
DTED	Digital terrain elevation data
ML	Machine Learning

CHAPTER 1

OVERVIEW

UAS safety, especially while landing, depends on accurate altitude estimation [1]. Various technologies help with this vital role, but each has its drawbacks. GPS-aided-AHRS is commonly used for navigation in commercial aviation [2]. However, its poor update rate, usually one PPS is unable to cope with the rapid descent requirements of the landing stage. Altitude data in GPS is referenced from MSL, while autonomous landing requires AGL altitude data. LiDAR systems find application in altitude estimation as well. However, they are limited in circumstances with low visibility such as heavy sleet, hailstorms, mist, or sandstorms [3]. Measurements using barometric sensors warrant recurrent corrections owing to temperature-induced changes in air pressure. Appropriately, RA emerges as the most optimal altimetry solution for UAS because of its rapid update rate and AGL altitude measurement. Its efficacy in adverse weather conditions allows for enhanced UAS safety since EM waves pass through atmospheric hindrances largely unaffected.

Two of the most popular waveform candidates for commercial RA are the Pulse Doppler and FMCW [4]. Since CW radars only estimate Doppler; their applicability for altimetry use case is miniscule [5]. Pulse Doppler RAs measure altitude by generating RF pulses of very short duration and tracking their round-trip delay. Therefore, the pulse period must be much less than the time it takes the pulse to travel from the generator to the target and reflect to circumvent temporal overlap. Additionally, the solid-state switching period to transition from Tx to Rx cycle is equally significant. LO instability expressed as PPM further exacerbates the timing requirements. Jointly, all these pieces imply a longer round-trip period which in turn impedes the RA from measuring very low altitudes. On the contrary, FMCW-based RAs can measure altitude without a lower bound due to the inherent ability of simultaneous transmission and reception. Since RA is most critical in the landing phase till touchdown, the FMCW waveform serves the purpose more aptly. Furthermore, the continuous transmission increases the average power leading to a reduced peak power. This is particularly crucial from a public health perspective to

regulate the maximum allowed instantaneous power. Contrarywise, pulsed-Doppler radars have a 10% transmission duty cycle. As a result, they must transmit more peak power than their FMCW counterpart to achieve the same average power.

The majority of mmWave automobile radars manufactured in the past decade used SiGe architecture with considerably large volume but limited control to tailor the parameters of waveform [6]. Over time, the unified 45 nm MMIC, also known as RFCMOS, has gained popularity by offering an all-in-one solution that integrates an MCU, DSP, HWA, and RFFE on the same chip [7]. This breakthrough has paved the way for highly flexible waveform design with brilliant performance in a small, affordable device. Their initial use case was ADAS in premium cars, but they now have transcended to use cases beyond the automotive realm [8]. Being a low-budget solution and ubiquity, academicians and engineers are always motivated to maximize performance and develop new strategies to push the boundaries of hardware constraints. One interesting use case for mmWave automotive radars could be the deployment of an RA for airborne platforms. UAS are becoming more popular by the day due to their massive application in everyday activities. Legacy RAs in civil aviation operate in the 4.2-4.4 GHz frequency region [9], [10]. With the emergence of 5G networks, there is contention for available spectrum in the cited frequency band and there is a need for pioneering approaches to fill this gap. mmWave automotive radars are a viable candidate however deviating from obstacle detection to terrain backscattering estimation necessitates a significant shift to realize an aviation-grade RA.

The commercial scope of mmWave radars for UAS altimetry is existent, however academic discourse is rather limited. This investigation seeks to fill the literature gap on the use of these radars for the intended application owing to waveform design convenience, inexpensiveness, and common availability. Aptly, the main objective is the appraisal of mmWave radars for UAS altimetry. Generally speaking, figures of merit for RAs include minimum and maximum altitude, HPBW of antenna, and measurement accuracy. The cited metrics are interconnected requiring a thorough understanding of compromises is crucial to fulfil their diverse operating needs. Adapting automobile radars for altitude estimation requires a two-tier approach to achieve the required performance. Firstly, theoretical and mathematical understanding of hardware limits and performance metrics. Next, evaluation of contemporary and

legacy signal processing algorithms for suitability in high-accuracy altitude measurement capability.

This study aims to start a new academic debate on mmWave altimetry for UAS covering the intricacies of performance metrics with the constraint of limited reference works. To the best of the author's knowledge, a comparable work with such details is unreported. Existing materials on automobile radars generally use complex mathematical formulations and theories that young researchers may find perplexing.

Although the reference MOPS of RAs for aviation are formidable, there is no restriction for extending the performance metrics to even greater extents. These enhancements have the potential to meet a diverse set of existing and forthcoming needs of altimetry in UAS. Moreover, there is immense potential for improving capabilities. Appropriately, this work comprises two discrete phases of the UAS flight profile including the cruise and landing approach. The following chapters justify the distinct operative requirements of both stages and then derive the resulting waveform specifications based on conceptual and quantitative breakdown. The rationale behind identifying these stages discretely is to establish the flexibility of the proposed waveform capable of meeting a wide range of operational needs.

The cruise stage denotes the standard flight segment of an aircraft during which it performs a designated role. During this stage, aircraft sustain a constant altitude AGL [11]. Appropriately, the focus is on achieving high altitude while upholding maximum possible accuracy. RAs are primarily employed in aviation for landing approaches [12]. Within the current context of industrial growth, there is an increasing inclination towards the use of small-sized UAS in many fields such as agriculture [13], law enforcement [14], and traffic control [15]. Simultaneously, ensuring the safety of these UAS is of equal importance, especially during the process of autonomous landing. Traditional RAs do not possess the ability to generate spatial information required to accurately determine the actual height directly beneath the aircraft along the radar's line of sight. For example, an item that reflects EM waves very well and is not directly in line with the measuring device may result in an incorrect altitude measurement [16]. Considering this constraint, it is suggested that the AoA can be utilized to estimate the actual altitude. The inclusion of this feature is expected to greatly enhance situational awareness and provide a greater level of aircraft safety. Two corner cases were simulated employing a small-sized VTOL drone landing on a concrete landing strip of

a ship surrounded by water. It is expected that the findings of this research shall supplement additional sensors on board during the landing phase.

The main goal of this research effort is to create a flexible waveform that offers improved range accuracy and precise altitude estimate, resulting in tangible benefits. Therefore, it is crucial to thoroughly explain the signal-processing elements associated with determining the altitude and AoA, while considering the limitations imposed by the hardware of automotive radar employed. The selected automobile radar utilizes a software-defined architecture, which enables the achievement of the targeted goal. Nevertheless, it is essential to rationalize operational requirements to prevent the establishment of excessively ambitious benchmarks. The key to solving this problem is to prioritize the appropriate performance statistic for each specific stage of the flight, while also considering the other metrics and making reasonable compromises. For example, fast update rate and fine range resolution hold little value in the cruise stage, but high-altitude estimation is a mandatory requirement. Conversely, during the landing phase, the prioritizes accuracy and update rate. From a SWaP perspective, having a radar that can switch waveforms adaptively is well-suited to the goal of enhancing operational durability across a wide range of UAS. To accomplish the above goals, the existing signal processing techniques from both past and present literature were examined. The radar toolbox in MATLAB [17] was used to simulate the flight stages. The simulation environment offers a wide range of choices for designing the FMCW waveforms and propagation utilizing phased array antennae. The hardware is responsible for generating and transmitting EM waves ensuing signal acquisition by the ADC. Afterward, the sampled data are subject to post-processing. From an administrative standpoint, this strategy is wasteful because simulating several scenarios for each flight stage entails massive overhead in terms of resources. Aptly, the proposed approach validated the scenarios through simulation leveraging the specifications of the automotive radar, AWR1843 [18]. This allows for seamless tuning of waveforms, resulting in substantial resource conservation. Eventually, the CFAR algorithm is utilized to determine the AGL altitude.

TDM-MIMO radars are widely used in automotive applications [19]. They employ virtual antennae to calculate the AoA. Conventionally, target detection comprises the use of fast-time and slow-time dimensions. Radar cubes offer a third dimension with the addition of multiple receive antennae [20]. Subsequently, signal processing

procedures are utilized to concurrently determine the range, Doppler, and angular information.

All three features are crucial within the scope of the waveform proposed in this work converse to legacy RAs that only report range information [21]. There is a general scarcity of academic discussions in the literature on the utilization of radar cubes RA use case.

The introduction of radial velocity component caused by aircraft ROD with respect to terrain and the variations in terrain profile pose a significant challenge that requires careful consideration during the waveform design stage. Appropriately, this text provides explanations in theory in tandem with mathematics to elaborate the Doppler compensation step. Thus far, there has been a dearth of in-depth discourse on this subject. The subsequent sections illustrate that, without a specific mandate to calculate the ROD, the resulting radial velocity component has no impact on altitude measurement, regardless of variations in the terrain profile. Furthermore, when accurately considered, it does not affect the AoA, even when implementing TDM-MIMO. Three commonly used variations of CFAR algorithms leverage particular parameters to optimize the trade-off between sensitivity and the PFA [22]. Therefore, it is crucial to select the most suitable CFAR version that meets the needs of both stages of the flight. To fill this gap, three popular CFAR variations have been assessed to enhance the detection accuracy for ground surfaces. The quantitative underpinnings and conceptual aspects of the aforementioned terminologies may appear intimidating to audiences coming from varied backgrounds. Fittingly, the manuscript is structured in a tutorial-style format. The manuscript is dissected into lucid and understandable ideas with the following contributions:

- Appraising the practicability of mmWave radars for altitude measurement in UAS.
- A straightforward, step-by-step guide focused on the conceptual and numerical foundations of performance metrics.
- Selection of appropriate clutter model followed by evaluation of ground surface backscattering with hardware specifications of chosen radar.
- Discussion on the MOPS of RAs used in aviation and the reasoning behind their repurposing for the UAS use case.

- Proposing a systematic methodology for deriving waveform specifications based on operational requirements.
- Presenting a simplified mmWave altimetry radar cube signal processing flow.
- Quantification and renumeration of Doppler induced by rapid ROD of UAS and terrain elevation.
- Enhanced situational awareness during UAS autonomous landing with TDM-MIMO.
- A seamless simulation of radar scenarios using the hardware specifications of AWR1843.
- Analysing standard variants of CFAR and discussing the rationale for choosing the optimal variant for the target use case.

The rest of the thesis is structured as follows: Chapter 2 encompasses a brief account of the history of mmWave automotive radars, regulations, potential avenues for growth, and associated limitations. A summary of related works is presented in Chapter 3 while the quantitative and conceptual analysis of performance metrics of FMCW radars is provided in Chapter 4. Chapter 5 comprises a systematic methodology for optimal design of waveform. The following Chapter 6 presents the preliminaries of signal processing for altitude estimation in RAs. Chapter 7 amalgamates the cruise stage while Chapter 8 covers the landing approach stage with associated discourse on enhancing AoA resolution using TDM-MIMO. Chapter 9 presents the author's discussion with a summary of the challenges endured so far and outlines the next phases of research. Chapter 10 concludes the thesis, while Chapter 11 includes the deliverables resulting from this research.

CHAPTER 2

RECENT ADVANCES, REGULATORY ISSUES, PROSPECTS, AND IMPEDIMENTS

This Chapter provides an overview of the recent advances in mmWave automotive radars. It touches upon regulatory issues, discusses opportunities and challenges, and concludes with the rationale behind selecting a particular radar chipset.

2.1. Recent Advances

Automotive applications of mmWave radar began in the 1970s. Scientists and organizations investigated distance radar for collision prevention, developing prototypes and applications. Integration, size, and cost issues delayed market acceptance until the late 1990s with the initial batch of 77 GHz vehicle radar sensors released to the market addressing both technological and cost-related challenges.

Integrated solutions were considered for automotive radars owing to volume and weight restrictions. To reduce hardware footprint, mmWave frequencies were studied. Making MMICs that could handle these high frequencies without losing RF performance was difficult. GaAs was used in early models for its outstanding RF performance, however, MMICs hampered the integration of digital logic. BiCMOS SiGe technology solved these problems by allowing digital logic circuitry integration and interoperability with regular silicon technologies. This development enabled miniatured, fully integrated radar sensors.

Recently introduced 45 nm RFCMOS MMICs combine strong RF and digital logic performance [7]. Since pure CMOS for effective power amplification at high temperatures was previously a major difficulty, this was a major advancement [23]. The extensive use of radars in ADAS enforcing mass production has led to the reduction of cost.

2.2. Contention in the Universal RA Frequency Band and Regulatory Aspects

RAs in commercial aviation have long operated in the 4.2–4.4 GHz band. Due to the spread of 5G cellular networks, the RAs suffer from receiver saturation [24]. Additionally, the relatively limited BW restricts fine range resolution, a topic discussed in ensuing chapters. To circumvent this issue, the mmWave regime emerges

as a viable avenue. The frequency range of 24 to 29 GHz offers a bandwidth of 5 GHz with great potential for range resolution. However, spectrum regulatory bodies in most countries, with a few notable exceptions, have had their bandwidth reduced to 250 MHz [25]. In light of the aforementioned issues, the 77-81 GHz band, with 4 GHz of useable BW, has surfaced as a lucrative alternative [26].

2.3. Prospects & Impediments

Operating in the 77 GHz band provides significant advantages, including a ninefold reduction in antenna size and a threefold improvement in velocity resolution due to the wavelength's relationship with the carrier phase. While velocity measurement isn't the primary focus of this study, Chapter 8 will demonstrate how enhanced velocity resolution can aid Doppler compensation during AoA measurements. Additionally, the wider bandwidth available in the 77 GHz range compared to 24 GHz enables a substantial twentyfold increase in range resolution. However, challenges such as higher noise figures and significant FSPL at shorter wavelengths [27] complicate the transition to this frequency range. These factors exacerbate the already low transmit power, resulting in a decreased SNR and a reduced radar range.

At higher altitudes, the reduction in SNR presents a significant challenge, necessitating innovative approaches for improvement. Traditionally, boosting Tx power and improving the gain of radiating elements could be possible solutions. Yet, these methods come with their trade-offs, including increased volume and higher costs. As outlined in Chapter 1, this study focuses on leveraging existing automotive radars for UAS altimetry without introducing modifications, as their SWaP characteristics make them ideal for this application. While conventional methods remain viable, it is important to recognize that beyond a certain point, increasing the power budget yields diminishing returns, since radar range is also influenced by IF filter bandwidth [28]. Moreover, Chapter 4 will illustrate that although FSPL limits radar range, backscatter from the ground surface tends to increase as the wavelength decreases.

2.4. Considerations for Chosing the Radar Chipset

Automotive radars are manufactured and mass-produced by famous automobile corporations around the globe. The attributes and performance metrics of these radar modules have been subject to qualitative and quantitative comparisons in the literature [29], [30]. However, these radars are not well-suited for academic research due to their simplified, out-of-the-box functionality, and owing to their modularity, they entail

high cost. In another study, the available radar sensors on the market were appraised in a side-by-side comparison. The findings of that review yielded that RFCMOS chipsets offer the maximum level of control in the waveform design process coupled with significant computational resources to house and run embedded software with a large footprint.

Major MMIC producers are now in the full-time manufacturing of RFCMOS technology. The disruptive flexibility offered by these chipsets through programmable FMCW chirp configurations, multiple antennae, and powerful DSP for signal processing allows for a single-chip solution for applications requiring a wide dynamic radar range. Interestingly, this aligns well with the requirement of RA for the UAS use case. Out of the available flavors in the market, this investigation makes use of the Texas Instruments, AWR1843 [31]. Its formidable capabilities from waveform design as well as signal processing perspective, very sound reference designs, and popularity amongst application engineers governed the pathway for this decision-making.

By the time this manuscript is available with open access, market players are poised to bring even more capable sensors on the horizon. A review was conducted to provide a reasonable comparison of RFCMOS-based radars [8]. Albeit, it provided a helpful resource for comparing the hardware specifications, it lacked substantial value in understanding how these systems perform in particular real-world use cases. At present, there is no reference study encompassing an assessment of chipsets based on their performance for the specific use case of altitude measurements in UAS. This endeavor does not claim to have conducted a comprehensive appraisal of all existent mmWave radar chipsets. Rather, it briefly outlines the rationale for chosing AWR1843 and presents a systematic methodology for the derivation of waveform within the hardware constraints of the radar.

CHAPTER 3

LITERATURE REVIEW & RELATED WORK

As previously mentioned in the introduction, application engineers and academicians are naturally inclined towards technologies that are widely applicable and cost-effective, surpassing inherent hardware limitations. Numerous significant quantitative and experimental investigations outside the scope of ADAS are prevalent in academic discussions. However, due to being a relatively new field of study, there is a scarcity of literature specifically focused on mmWave altimetry that may be used as a direct reference. The methodology offered in this investigation was carefully orchestrated after conducting a comprehensive assessment of available works, in accordance with the goals of this project. The ensuing sections provide an abridged coverage of the literature that formed the foundation of this research endeavor.

3.1. Reference Studies on Automotive Radars for Non-Conventional Applications

The dissertation in [32] exemplifies the endeavor to broaden the applications of automobile radars within the scope of traditional limitations. The referenced study established the groundwork for addressing the uncertainty in velocity estimation much beyond the maximum measurement capabilities of automotive radars. Additionally, challenges and opportunities in estimating the RCS of a 9mm bullet using automotive radars were presented in [33]. Likewise, a comprehensive framework was proposed for vital signs [34]. Collectively, these investigations establish the foundation for investigating the unexploited capabilities of these radars. In light of these efforts, this work propels the debate for evaluating the previously uncharted potential of automotive radars for use in RA of UAS.

3.2. Legacy & Contemporary Works

Historically, radar technology was primarily used for military purposes, supported by extensive research and development. Over time, its applications have expanded significantly, leading to the creation of various academic resources, including textbooks covering radar concepts, principles, algorithms, waveforms, and systems [35], [36]. With modern advancements, such as TDM-MIMO radar

techniques, it has become more practical to consult technological surveys and review articles [37] – [39]. These sources offer valuable insights into industry trends and future research directions but often provide only a broad overview rather than detailed analyses. In contrast, mmWave radar manufacturers have released whitepapers and application notes targeted at application engineers [40] – [42]. While these documents cover the basics of product development, they provide limited introductory information and minimal experimental detail.

The purpose of this thesis is to close the gap by incorporating the positive aspects of many genres of writing that already exist. A method that is based on tutorials and provides both theoretical insights and practical comprehension of cutting-edge technologies is the goal of this endeavor. To this end, theoretical foundations have been derived from famous textbooks, and application notes have been used to clarify the capabilities of the hardware. Even though other works have provided in-depth mathematical insights into 3D signal processing in mmWave automobile radars [43], this thesis takes a tutorial-style approach that is specifically tailored to altitude measurement in UAS.

3.3. Reference Works Employing mmWave Radars for UAS Applications

Research endeavors using mmWave radars to enhance flight performance in commercial drones are well-documented in the literature. DL techniques are commonly applied across various domains, including autopilot systems, object detection, and flight navigation [44] – [46]. Particularly relevant to this work is a study focused on estimating altitude using a VTOL drone [47]. In this study, the CFAR algorithm was utilized for terrain sensing, but the measurements were not thoroughly characterized, and there was a general lack of quantitative analysis. Another study explored the use of mmWave radars for AGL height estimation, but it prioritized application aspects over detailed analysis [48]. To the best of the author's knowledge, the most pertinent experimental approach to AGL altitude measurement was presented in [49]. This study estimated altitude using a 77 GHz mmWave FMCW radar chipset, employing an improvised CFAR with an empirical noise threshold instead of an automatic evaluation of noise threshold. Additionally, a range adjustment method was proposed to enhance consistency in low-altitude measurements. This referenced work served as inspiration for this thesis, demonstrating that mmWave automotive radars can effectively estimate altitude. However, it did not discuss the details of clutter.

3.4. mmWave RAs in the Commercial Sphere

RA solutions based on mmWave automobile radars have recently gained traction in the commercial sphere use on UAS [11]. The presence of such products validates the importance of this body of work. For comparative studies and mapping of theoretical findings, the technical specifications of these radars are of great significance. However, it is worth mentioning that the aim of most commercial ventures is not intended for academic or scientific contribution. To address this niche, this thesis presents a complete academic framework for constructing a mmWave RA for UAS from scratch.

3.5. Inherent Constraints of Conventional RA

In the aviation industry, MOPS govern the development of RAs such as the ED-30 [50] and DO-155 [51]. The criteria listed in these documents have stayed mostly unchanged for 50 years. The rudimentary requirements listed in these standards have stood the test of time and remain applicable for comparatively straightforward landing situations in commercial aviation. To this day, no specialized MOPS for RAs has been categorically formulated for the UAS use case. Thus, the cited standards served as ab

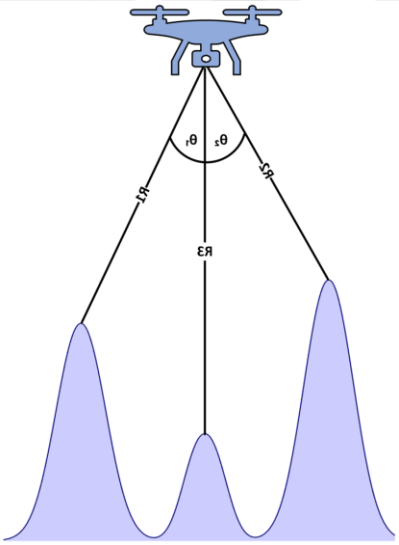

Figure 3.1 Ambiguity in Altitude Measurement [52]

initio for pushing the case for mmWave RA in UAS. Per the existing aviation standards, HPBW is a critical performance parameter. However, as a consequence, when a scatterer at an off-boresight angle from the axis of the radar antenna offers a strong reflection, it causes an inaccuracy in measuring the altitude directly beneath the airframe.

A cross-section view of a terrain patch is shown in Figure 3.1. The altitude estimation is ambiguous, making it difficult to ascertain the actual altitude. Specifically, in the case of compact VTOL drones depending merely on RA for landing, such inaccuracies can result in harmful consequences. Likewise, in terrain investigation expeditions where maintaining a consistent AGL is mandatory throughout rugged terrain, traditional RAs are likely to produce inaccurate results. Given the growing use of UAS in various commercial fields, it is becoming increasingly important to focus the discussion on mmWave altimetry, with the capacity to estimate the AoA.

3.6. Prevalence of TDM-MIMO in Automotive Realm

TDM-MIMO increases AoA estimation angular resolution by leveraging the concept of virtual antennae while using significantly fewer physical antennae [53]. Due to its excellent SWaP features, it is used in car safety applications to avoid obstacles, ensure pedestrian safety, and detect other vehicles [38]. Although state-of-the-art reviews provide significant insights into industry trends and research goals, they frequently lack thoroughness. Furthermore, the instructional resources provided by radar manufacturers, such as application notes, typically emphasize implementation considerations and only provide a basic understanding of theoretical principles [40]. As a major portion of this manuscript entails signal processing, the study in [43] is an important and useful reference. This study utilizes a comparable and efficient approach but limits the focus to altitude measurement in UAS.

3.7. Legacy Use of CFAR for Terrain Sensing

The CFAR method is routinely employed for target detection in the automotive domain [54]. The application of CFAR for terrain sensing has been the subject of reports in the published literature [55]. Nevertheless, the referenced study lacks a solid mathematical basis and fails to thoroughly investigate performance aspects. A separate study examined the efficacy of radar sensors in estimating AGL altitude, with a primary emphasis on potential applications and offering limited in-depth analysis [56]. The study that most corresponds to the altimetry use case employed a mmWave radar using FMCW to determine the altitude of a VTOL drone from the ground with reasonable accuracy [49]. The mentioned study also utilized an improvised version of CFAR for terrain sensing. Extensive research has been conducted to analyze and describe the effectiveness of several types of CFAR algorithms [57]. Nevertheless, no comprehensive analysis has been undertaken to compare their effectiveness in UAS

altimetry, whether in simulated settings or real-world experiments. The objective of this paper is to address this deficiency by conducting a comparison of different CFAR variations inside a simulated environment. Furthermore, it explores the rationale for choosing the most suitable option to fulfil the specific requirements of a certain phase of a flight.

3.8. Reference Blueprints and Simulation Framework

The implementation aspects of time-domain windowing, spectral analysis using FFT, CFAR, and arrangement of data in radar cube, were obtained from the TI SDK for mmWave radars [58]. Nevertheless, these references lack scholarly merit. To fill this void, the remaining sections include theoretical and mathematical discussions. The MathWorks Radar Toolbox [17] was used to simulate radar scenarios, while the Phased Array System Toolbox [59] was utilized to construct the FMCW waveform. The simulations assumed a LoS model, without the effect of reflections.

CHAPTER 4

A PRIMER ON PERFORMANCE METRICS IN FMCW RADARS

This work aims to deliberate the operational needs of RA for altitude measurement in a broad range of UAS types courtesy of the excellent SWaP features of mmWave radars. Particularly, small VTOL drones are expected to benefit the most given their limited capacity to carry sensor payload. Nevertheless, mmWave RAs are a suitable fit for larger aircraft as well. In light of the aforementioned utility, a primer on fundamental concepts associated with FMCW-based mmWave RA is crucial. The following subsections cover the quantitative and qualitative aspects concerning performance metrics while drawing insights from [28], [32], [35], [36], [41], [42] along with the authors' observations.

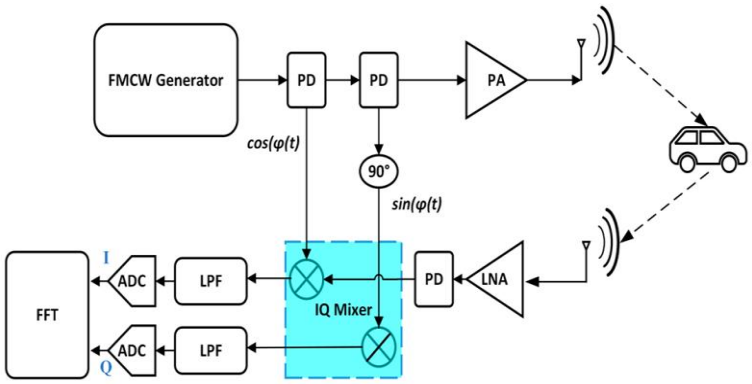

Figure 4.1 Block Diagram Exhibiting Components of an FMCW Radar [34]

The conceptual framework of FMCW radars is conveniently explained in the following text using quantitative expressions within the limits of AWR1843. The basic building blocks of an FMCW radar are elucidated in Figure 4.1. It must be noted that both real and complex baseband models are prevalent in FMCW however for the sake of this study, a complex I/Q architecture was adopted. The rationale for this choice is explained in Chapter 5. Similarly, there are many variants of the modulation type in FMCW radars. For the sake of simplicity and provision in the AWR1843, LFM was

chosen in this investigation. The time-dependent frequency, $f(t)$, in an LFM waveform is mathematically expressed as

$$f(t) = f_c + St, \tag{1}$$

where f_c is the resting frequency and S is the time rate of change of frequency. This waveform spanned over a time period, T_c is referred to as chirp shown in Figure 4.2 with BW, B, expressed as

$$B = ST_c. \tag{2}$$

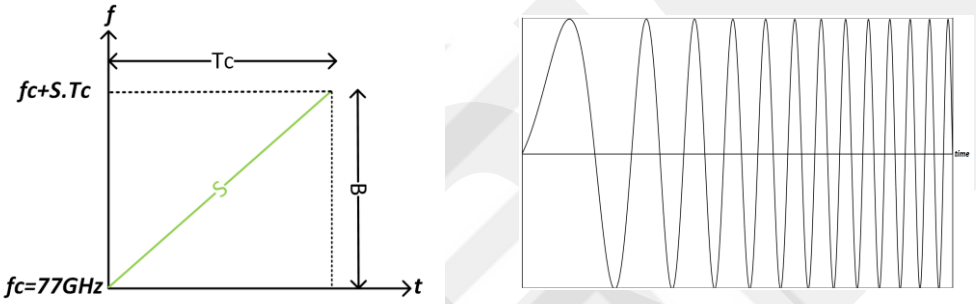

(a) (b)

Figure 4.2 (a) Spectrogram of an FMCW Chirp (b) LFM in Time Domain [41]

4.1. Range

FMCW radars operate on the principle of RTOF of EM waves. The waveform is generated and emitted which reflects off targets with the antenna FOV. The received carrier is multiplied by the instantaneous frequency of the generator resulting in sum and difference terms.

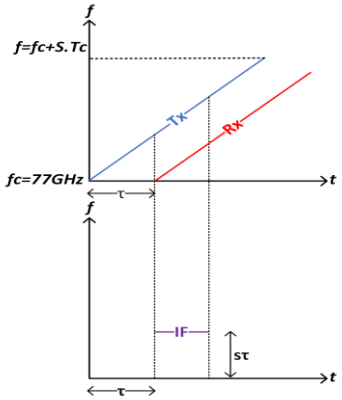

Figure 4.3 IF SignSal Generation [41]

Afterward, the high-frequency term can be suppressed using a low-pass filter while allowing the difference term known as the IF signal containing beat frequencies. Figure 4.3 demonstrates the overlap between Tx and Rx chirps and the resultant IF signal. It is pertinent to discuss the mathematics behind the generation of IF signal. The term f_c has been deliberated omitted to simplify the mathematical expression. The instantaneous frequency of the Tx chirp can be expressed using the line equation as

$$f_{Tx}(t) = St. \tag{3}$$

Similarly, the instantaneous frequency of Rx chirp is given by

$$f_{Rx}(t) = St - S\tau. \tag{4}$$

where τ is the RTOF of the EM wave and also the x-intercept of the Rx chirp. Taking the difference of (3) and (4) comes out to be

$$f_{IF} = f_{Tx}(t) - f_{Rx}(t) = S\tau. \tag{5}$$

Eq (5) gives a meaningful insight that f_{IF} is not a time-based function and depends only on S and τ. Using the velocity of EM waves, c, the RTOF for a target at range R can be estimated using the second law of motion as

$$\tau = \frac{2R}{c}. \tag{6}$$

Eq(5) can then be expressed using (6) as

$$f_{IF} = \frac{2SR}{c}. \tag{7}$$

4.2. Maximum Range & Finest Range Resolution

As indicated by (7), f_{IF} is proportionate to R. However, this relationship is limited by the BW of the IF filter. In automotive radars designed for long-range applications, such as cruise control, the IF filters are typically optimized for ranges up to a few hundred meters [60]. Rearranging (7), the maximum range is given as

$$R_{max}(IF_{max}, S) = \frac{cIF_{max}}{2S}, \tag{8}$$

The constraint of limited IF filter bandwidth was discussed in Chapter 2. However, this constraint can potentially be compensated for by reducing the chirp slope. It is essential to introduce the concept of range resolution at this point before delving

further. It is the ability of a radar to resolve two distinct targets into unique range bins. A signal in the time domain that has a longer duration is bound to have a finer spectral resolution [61]. In the case of FMCW radars, the observation window is T_c. Accordingly, the spectral resolution can be expressed as

$$\Delta f_{IF} > \frac{1}{T_c}, \tag{9}$$

By using (9) in (7), an inequality can be derived as

$$\frac{2S\Delta R}{c} > \frac{1}{T_c}. \tag{10}$$

$$\Delta R > \frac{c}{2ST_c}. \tag{11}$$

Using (2), expression (11) can be rewritten as

$$\Delta R(B) > \frac{c}{2B}. \tag{12}$$

Equation (12) implies that the range resolution of an FMCW is only dependent on the bandwidth of the chirp used in the transmission.

4.3. Link Budgeting

As already cited in Chapter 2, the IF BW and SNR both affect the maximum range. Even if the beat frequency falls within the IF filter bandwidth, a low SNR can compromise the achievable range. It's essential to estimate this carefully in practice. The radar range equation can be rearranged for received power as [5]

$$P_r = \frac{P_t.G_t.G_r.\sigma.\lambda^2}{(4.\pi)^3 R^4}, \tag{13}$$

where the wavelength is denoted by λ, P_t is the emitted power from the monostatic radar. G_r and G_t are the Rx and Tx gains of the antennae respectively with σ being the RCS. It is important to realize that σ is the RCS of a point target whilst for case of terrain sensing applications like altimeter, equation (13) needs to be extended with RCS for surface of the terrain expressed as

$$\sigma = \iint_{A_{ill}} \sigma_o . dA = \sigma_o . A_{ill}, \tag{14}$$

where σ_o is the coefficient of backscattering per unit area referred to as the NRCS [62]. Estimating NRCS involves empirical research and is beyond the scope of this thesis.

The objective here is to use a generic analytical model to provide an approximation. The models employed in this investigation may not be a suitable fit for remote sensing, since little attention is attributed to scatterers. However, for a RA application, the NRCS at a grazing angle, ψ >40° can be represented as the total of the clutter resulting from low grazing angles and specular scattering [63]:

$$\overline{\sigma_0(dB)} = \overline{\sigma_{9.3G}} + 10\,log_{10}\left(\frac{0.65e^{-tan^2(90-\psi)/tan^2(ß_0)}}{tan^2(ß_0)}\right) + 10\,log_{10}\left(\frac{f}{9.3}\right) + 10log_{10}(0.1\psi), \quad (15)$$

where f is the frequency in the 77 to 81 GHz band, $\overline{\sigma_{9.3G}}$ represents the mean NRCS at 9.3 GHz frequency for ψ<10°, $\tan^2(ß_0)$ signifies the RMS of the terrain elevation. The inclusion of the term (0.1ψ) takes into consideration the impact of raising ψ above 10°. The mathematical statement includes the NRCS at 9.3 GHz because the experiments were conducted at this frequency. To render the model generic, extrapolations were applied. To estimate backscattering RAs, such generic models suffice the requirement. Equation (15) might appear complex mathematically, but it simply indicates an increase in ground surface backscattering with higher frequencies due to reduced absorption and increased reflection at larger grazing angles. Moreover, interested readers are encouraged to consult [62] – [64] for a more comprehensive discussion and deeper insight into clutter estimation from ground terrains. The Mathworks documentation on clutter also utilizes the same model for look-down cases with frequencies in the mmWave regime [65]. This situation makes up for the high FSPL with a higher value of NRCS. It is now appropriate to shift the debate toward the evaluation of A_{ill}. It is the projection of the radar antenna on the terrain due to its HPBW in both E and H planes [66] as shown in Figure 4.4. It is a function of the beam area A_{beam}, and the angle of incidence, θ_i expressed as

$$A_{ill} = \frac{A_{beam}}{cos(\theta_i)}. \quad (16)$$

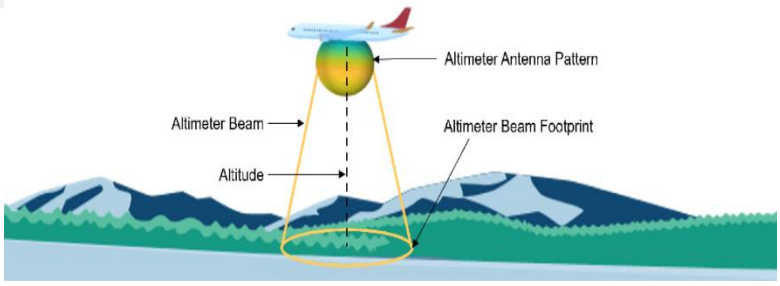

Figure 4.4 The footprint of Antenna Beam on Terrain [67]

Given A_{beam} is an elliptical projection, (16) can be expressed as

$$A_{ill} = \pi \frac{\theta_e}{2} \frac{\theta_a}{2} R^2 sec(\theta_i), \tag{17}$$

where R is the altitude and θ_e and θ_a sifnigy the E and H plane HPBW of the radar antenna expressed in radians respectively. The term $sec(\theta_i)$ approaches to unity for the RA use case. Having calculated both the required terms for evaluation of RCS, the discussion ensues for the calculation of maximum measurable altitude. SNR is a critical figure of merit that directly governs the maximum altitude. It is the ratio of the received signal power to the noise power. After providing the expression for received signal power in (13), the next step is to express the noise power, P_n in watts as

$$P_n = k_B T B_n F, \tag{18}$$

where F is the NF of the receive chain, T is the receiver temperature expressed in degrees Kelvin, k_B is the Boltzmann's constant and B_n is the bandwidth of thermal noise. Noise bandwidth estimation must be explained with great care since misapproximation can lead to a non-optimal waveform design. Accurate noise estimation requires knowledge of the precise stage at which noise is to be tapped. Figure 4.1 illustrated a dual channel IF filter followed by independent ADCs for I and Q. After the sampling stage in ADC, the signals are subject to FFT.

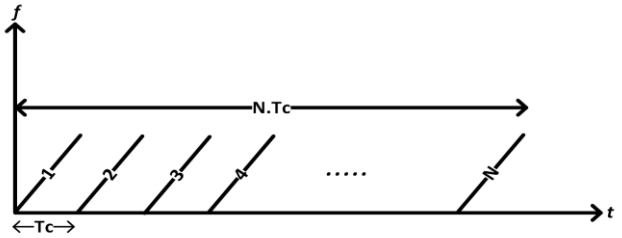

Figure 4.5 FMCW Chirp Frame [41]

The FFT stage resolves the time domain signal inclusive of the thermal noise into frequency segments denoted as bins. The noise level per frequency bin is governed by an inverse relationship with the observation window, T_c [41], [68]. Doppler estimation is not the main goal in RAs but multiple chirps can be aggregated into a chirp frame for SNR enhancement. An FMCW chirp frame is elucidated in Figure 4.5 with a total of N chirps. This allows for an increase in the observation time collectively denoted by, T_f, expressed as

$$T_f = NT_c. \quad (19)$$

The noise bandwidth per frequency bin can then be estimated as

$$B_n = \frac{1}{NT_c}. \quad (20)$$

Plugging (20) into (18), the modified expression for P_n becomes

$$P_n = \frac{k_B TF}{NT_c}. \quad (21)$$

The updated noise power expression follows the zero-mean Gaussian distribution of its PSD, which implies that noise tends to be minimized as the observation interval gets longer. The maximum range is achieved in a radar system when the minimum detectable power, $P_{r_{min}}$ is available at the receiver. This threshold is provided by the manufacturer against an acceptable value of PFA at the minimum possible signal to noise ratio termed, SNR_{min}. For the sake of this investigation, this threshold was taken from the manufacturer's manual of AWR1843 [21]. Using (20), $P_{r_{min}}$ can be expressed as the sum of P_n and SNR_{min} as

$$P_{r_{min}} = \frac{k_B TF}{NT_c} + SNR_{min}. \quad (22)$$

Using equations (14), (17), and (22), the final form of radar range equation formulated for maximum range can be expressed as

$$R_{max}(SNR_{min}) = \sqrt{\frac{P_t G_t G_r \sigma_o \theta_e \theta_a \lambda^2}{\left(\frac{k_B TF}{NT_c} + SNR_{min}\right) 256\pi^2}}. \quad (23)$$

CHAPTER 5

A SYSTEMATIC METHODOLOGY FOR WAVEFORM DESIGN

Having discussed preliminary performance metrics, this chapter proposes a systematic methodology for waveform design. As already explained, in the absence of MOPS of RA in UAS, RTCA DO-155, and EUROCAE ED-30 have been deployed in commercial aviation for over five decades [50], [51]. Similarly, is a similar standard with minor modifications. However, there is no dedicated reference specifically tailored for RAs of UAS, making a one-to-one mapping of all requirements from these standards impractical. Moreover, contemporary RAs operating in the 4.2−4.4 GHz band that are employed in the aviation industry provide useful benchmarks for comparison of performance metrics [69]. Modern RAs using FMCW in the mmWave band have recently emerged. They are tailor-made for a broad range of UAS in terms of airframe size and provide high data refresh rates and dynamic altitude measurement capability [11]. These reference systems collectively lay the foundation for developing an mmWave FMCW RA with comparable performance. Since reliability and ruggedization from a product perspective are outside the context of this thesis, only the technological aspects have been deliberated. With this in mind, the primary performance metrics of interest are limited to altitude accuracy, maximum and minimum measurable altitude, and data refresh rate.

5.1. Update Rate Requirement

The update rate is not listed as a requirement in the MOPS of RAs for commercial aviation. Rather, there is a particular emphasis on antenna HPBW as a critical requirement. To the best of the author's understanding, between two consecutive radar sensor updates, the platform must not cover a longitudinal distance greater than the major axis of the elliptical projection of the antenna on the terrain. Accordingly, the antenna HPBW in both planes should be sufficiently large to accomplish this. It makes no difference which way the antenna is oriented for a radiation pattern that is symmetrical in both planes.

The radar platform under consideration for this investigation is the AWR1843BOOST having an azimuthal HPBW greater than the elevation plane counterpart [18]. The following quantitative formulas take this into account appropriately, and it was deemed advantageous to mount the antenna such that its azimuthal axis lines up with the longitudinal axis of UAS motion. The rationale behind this decision was based on the fact that the requirement to update frequently is most critical when UAS is traversing in the longitudinal direction. From (17), the major axis, D increases with an increase in the altitude, R. The quantitative expression can be given as

$$D = \frac{\theta_a}{2} R. \tag{24}$$

The maximum longitudinal velocity V_{max} and minimum measurable altitude, R_{min} govern the maximum temporal blanking between successive updates expressed as

$$\Delta t_{max} \leq \frac{\frac{\theta_a}{2} R_{min}}{V_{max}}. \tag{25}$$

According to this upper limit, a certain amount of time, Δt_{max} maybe allowed between each set of altitude measurements until the terrain surface overlap of elliptical antenna projections approaches zero. Aptly, the minimum required update rate, U_{min} is the multiplicative inverse of this duration gives as

$$U_{min} = \frac{1}{\Delta t_{max}}. \tag{26}$$

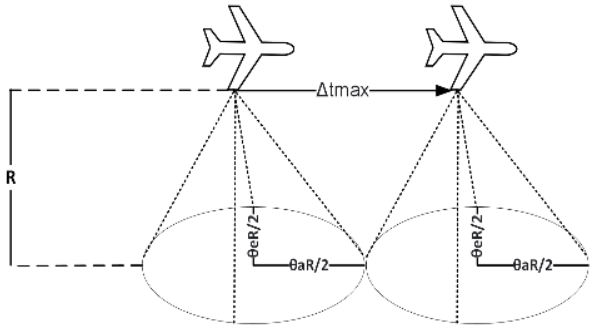

Figure 5.1 The Concept of Minimum Required Update Rate

The main point to be grasped is that the projection of the antenna on the terrain shrinks as the height of the platform reduces, which necessitates that altitude information must be updated more often. This trend is especially prevalent during the landing stage.

Additionally, the higher the platform speed, the higher the update rate requirement. The central idea covered in the aforementioned discussion is elucidated in Figure 5.1.

5.2. The Subtle Intricacy of Range Resolution & Accuracy:

True altitude reporting across altitude levels is possible with finer range resolution. A coarse range resolution is bound to introduce uncertainty within a specific range bin. According to aviation requirements, the range accuracy must be within ±1.5 ft, or in other words, a 3 ft range resolution. There is significant room for improvement as far as the lower limit of measurable altitude is concerned in the legacy RAs. A large distance must be maintained between the Tx and Rx antennae to prevent signal coupling owing to the large wavelength in the 4.2−4.4 GHz band. This situation is particularly unsuitable for small VTOL drones owing to very small airframes and limited capacity to carry sensor payloads. To address this challenge, the shorter wavelength in the mmWave regime allows for closely packed Tx and Rx antennae. This in turn allows for a much lower minimum measurable altitude. However, the benefit of the offering holds no value if the range resolution is very coarse because if the terrain surface lies in the very first range bin, the altitude may be regarded as zero. Given the proliferation of VTOL drones in a wide spectrum of everyday applications mmWave RAs hold great relevance particularly for traffic management in smart cities [70].

5.3 Dynamic Range of Altitude Measurement

This sub-section entails the discussion on the quantitative derivation of minimum and maximum measurable limits of altitude. The lower limit is influenced by the range resolution. Single-chip radar offers a software interface for programming a high-pass filter in the receive chain immediately before or after the low-pass filter. The purpose is to prevent coupling from the Tx chain from interfering with the Rx chain. This limitation is specific to FMCW radars since Tx and Rx circuits operate concurrently. Owing to a very short wavelength and very fine range resolution, despite the antennae being distanced by an order of multiple wavelengths, even a high pass filter with a very low cut-off frequency can be conveniently deployed. Similar to the maximum range, range resolution simultaneously depends on physical and signal processing constraints [28], [41]. It is expressed as

$$\Delta R(F_s, N_{FFT}, S) = \frac{cF_s}{2SN_{FFT}}. \quad (27)$$

where F_s is the number of samples per second, S is the rate of change of frequency termed the slope of the FMCW chirp and $N_{FFT}$is the order of FFT.

The aforementioned debate begs the question of why separate equations (12) and (27) for range resolution exist. Both equations are applicable depending on how the problem statement is viewed. Considering (12) is a physical limitation, it is the inherent ability of waveform to resolve targets into neighboring bins. However, the entities in (27) must be chosen such that limits defined by (12) can be achieved. Essentially, an FFT of sufficient order must be part of the signal processing chain to allow for a spectral resolution capable of providing high accuracy. Range resolution can then be given as a maximization function of (12) and (27) as

$$\Delta R \geq Max\left(\frac{cF_s}{2SN_{FFT}}, \frac{c}{2B}\right). \quad (28)$$

Continuing with the discussion on minimum measurable altitude, it is pertinent to not consider the initial m range bins. The rationale for this operation is to ensure that signal coupling does not affect the altitude measurement. The value of m depends on the displacement, Δx between the Tx and Rx antennae mathematically expressed as

$$m = Roundup\left(\frac{\Delta x}{\Delta R}\right), \quad (29)$$

where $Roundup$ refers to the process of rounding a decimal to the smallest integer greater than or equal to the input value. Equation (28) implies that range resolution is directly related to the sampling frequency F_s. The complex baseband architecture provides an ingenious workaround for the Nyquist sampling theorem [71]. Essentially, side-by-side processing of I/Q samples fulfills the Nyquist sampling criterion and the sampling rate requirement is effectively halved [72]. The lower limit of altitude that can be measured by the radar, Alt_{min}, is lower bound as

$$Alt_{min} \geq m\Delta R. \quad (30)$$

In the mmWave regime, R_{min} can be reduced to a much lower degree than the limits prescribed in MOPS of RAs for commercial aviation. The relatively laxed limits listed in the standards are well suited for commercial aircraft however small VTOL drones are expected to pose stricter demands. The radiation profile of an antenna is predictable

only outside the Fresnel region [73]. This puts yet another lower bound on the mandatory separation, Δy between the Tx and Rx, antennae expressed in terms of the largest dimension of the antenna, L as

$$\Delta y \geq \frac{2L^2}{\lambda}, \tag{31}$$

This lower bound has a higher limit for the contemporary RAs working in the 4.2-4.4 GHz owing to a larger value of λ since a higher cut-off frequency high-pass filter is mandatory to suppress the coupling signature. This finding further establishes the case of mmWave RAs. The architecture of AWR1843 comprising of microstrip patch antennae operating with very short wavelengths allows for compact packaging of multiple antennae on the same PCB, relaxing the lower bound in (31). There is yet another expression for maximum range as a function of N_{FFT}, given as

$$R_{max}(N_{FFT}, \Delta R) = N_{FFT}.\Delta R. \tag{32}$$

It is evident from (32) that increasing range and resolution at the same time is not possible, even when SNR and IF_{max} are not limiting the maximum range. Using (8), (23), and (32), an upper bound for the maximum range is expressed as

$$R_{max} \leq \text{Min}\,\{R_{max}(N_{FFT}, \Delta R), R_{max}(SNR_{min}), R_{max}(IF_{max}, S)\}. \tag{33}$$

5.4. Deriving the Waveform

Open-ended evaluation results in an underdetermined optimization problem with too many unknowns since the maximum range and range resolution are governed by a plethora of interdependent variables. This approach contradicts the systems engineering paradigm. To present a formidable methodology for deducing waveform specifications, a practical scenario is investigated. It is only reasonable to understand that the waveform specifications are governed by the requirements of the UAS and not the other way around. To this end, the operational requirements of a test UAS and hardware specifications of AWR1843BOOST [18], the breakout board of the AWR1843 radar are listed in Tables 5.1 and 5.2 respectively.

Table 5.1 Operational Requirements for mmWave RA

Requirement	Value	Remarks
SNR_{min}	20 dB	Minimum SNR Requirement
Accuracy	±0.45 m	Range Accuracy
R_{min}	1 m	Minimum Range Requirement
R_{max}	500 m	Maximum Range Requirement
V_{max}	20 m/s	Maximum Platform Velocity
T	273.15 °K	Temperature in Degree Kelvin

Table 5.2 Hardware Specifications of AWR1843BOOST

Requirement	Value	Remarks
$tan(ß_0)$	0.14	RMS of Terrain
F	15 dB	Noise Figure of RFFE
θ_a	56°	HPBW Azimuth
θ_e	28°	HPBW Elevation
f	77 GHz	Base Frequency
λ	3.9 mm	Wavelength
G_t	10.5 dBi	Tx Antenna Gain
G_r	10.5 dBi	Rx Antenna Gain
P_t(dBm)	12.5 dBm	Tx Power

Table 5.3 Waveform Specifications

Parameter	Value	Remarks
Δt_{max}	26 ms	Data Update Interval
U_{min}	38 Hz	Lower Limit of Update Rate
T_c	1 ms	Chirp Time Period
S	1.91 MHz/µs	Slope of FMCW Chirp
B	1.91 GHz	FMCW Chirp BW
$\Delta R(B)$	0.07 m	Function of BW
$\Delta R(F_s, N_{FFT}, S)$	0.85 m	Function of Slope
N_{FFT}	1024	FFT Order
Alt_{min}	0.85 m	Minimum Measurable Altitude
Alt_{acc}	0.85 m	Altitude Accuracy
N	16	FMCW Chirp Frame Size
T_F	16 ms	FMCW Chirp Frame Period
B_n	62.5 Hz	Noise BW
P_n	-141.27 dBm	Noise Power
σ_0	2.47	NRCS
$R_{max}(SNR_{min})$	4548.9 m	Function of SNR Requirement
$R_{max}(IF_{max}, S)$	783.3 m	Function of Maximum IF BW
$R_{max}(N_{FFT}, \Delta R)$	870.4 m	Function of FFT Order
Alt_{max}	783.3 m	Maximum Measurable Altitude

Table 5.3 details the resultant waveform and radar specifications. A careful comparison with reference systems and standards coupled with quantitative analyses shows tremendous potential [11], [50], [51], [69]. It is pertinent to note that the waveform specifications are derived systematically, starting with the maximum delay between data updates and culminating with the upper limit of the altitude to be measured.

CHAPTER 6

PRELIMINARIES OF SIGNAL PROCESSING

6.1. Summary of Performance Metrics

To provide ease of reference throughout the article, all performance measures are gathered in one place to ensure comprehensiveness. These metrics are essential mathematical expressions inherent to mmWave FMCW radar systems. A concise summary is presented in Table 6.1.

Table 6.1 Summary of Performance Metrics

	Range	**Velocity**	**AoA**
General Expression	$R = \frac{cf_{IF}}{2S}$	$V = \frac{\lambda \Delta f}{4\pi T_c}$	$\theta = \sin^{-1}\left(\frac{\lambda \Delta f}{2\pi d}\right)$
Resolution	$\Delta R = \frac{c}{2B}$	$\Delta V = \frac{\lambda}{2T_f}$	$\Delta\theta = \frac{2}{N_{Rx}}$
Upper Limit	$R_{max} = \frac{cf_s}{2S}$	$V_{max} = \frac{\lambda}{4T_c}$	$\theta_{max} = \sin^{-1}\left(\frac{\lambda}{2d}\right)$

All the terms listed in Table 6.1 have been cited in the text already except d and N_{Rx} which represent the antenna spacing and number respectively.

6.2. Typical Signal Processing in Automotive FMCW Radars

This work aims to leverage the usage of existing hardware and software packages employed in modern automotive radars. The purpose is to extend their functionality for possible fit to altitude measurement in UAS. Appropriately, the spatial dataset is a good initial step in establishing the basis for further stages. A spatial data set represents the spatial and kinetic characteristics of targets in a radar FOV. Obtained from measurements of range, velocity, and angle data, it generates a 3D depiction of the surroundings [74]. The fundamental process remains relevant, however the implementation details do not correspond precisely. The primary objective of altimetry is not to ascertain the platform's radial velocity with respect to the terrain but to provide a singular range value representing altitude. The methodology employed in this study involves utilizing as much reference information as possible from current studies to concentrate efforts on unexplored areas rather than

duplicating existing information. The term spatial data set is used interchangeably with point cloud. Figure 6.1 elucidates the series of stages involved in orchestrating a point cloud. It is crucial to emphasize that this model is generic and not specifically designed for an RA.

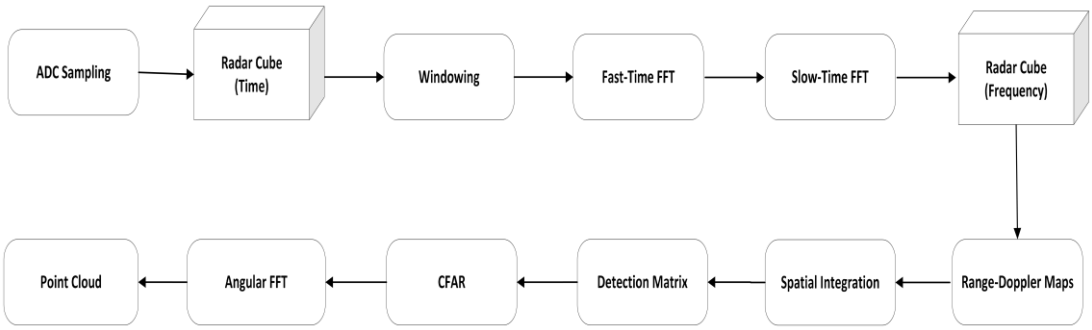

Figure 6.1 General Flow of Operations for Spatial Dataset Generation [75]

The rationale for discussion on preliminaries at this juncture is to present the most efficient FMCW waveform. Conventional RAs are designed exclusively for the measurement of altitude comprising one chirp in every radar frame with a singular Tx-Rx antenna pair. This configuration is inadequate for AoA and Doppler calculation since a minimum of two receiving antennas and two Doppler chirps are mandatory to achieve these capabilities, respectively. Employing numerous chirps and multiple antennae in a frame boosts the SNR. It was apprised in Chapter 2 that regulatory bodies have capped the maximum allowed Tx power for automobile radars. Aptly, these adjustments are necessary to recompense for signal attenuation due to the very short wavelengths in the mmWave regime [42]. Afterward, the second layer of FFT results in a non-coherent integration causing an increase in SNR as a function of the number of Doppler chirps.

6.3. Arrangement of Data in Radar Cube

Chapter 4 of this work has already covered the conceptual framework surrounding FMCW radars. This chapter now covers the series of operations immediately from that point on. An effective and practical way to store digital samples of IF signal is via a radar cube. This study does not cover the deep intricacies of managing memory in radar chipsets. However, for a more thorough understanding, interested readers might consult the DSP implementation guide [76]. The data arrangement in radar cubes is appropriate for carrying out signal-processing tasks on DSP. Moreover, it creates a visually convenient representation of space-time information. 3D target attributes

along with velocity information can be seamlessly extracted [77]. It must be noted that the frequency and time radar cubes used are not the same. While ADC samples are present in the time-domain radar cube, the spectral cube contains the 2D detection matrices per receiving antenna.

Figure 6.2 illustrates a legacy radar cube in the temporal domain. Each cell in the 3D matrix represents a complex sample of the IF. The horizontal axis is termed the fast-time dimension, directly related to range measurement. The terminology is such because it refers to the high sampling necessary to acquire the information embedded as beat frequencies in the IF signal. Likewise, the vertical cells correspond to the Doppler chirps with the time duration of columns known as the PRI. Since PRI is typically far longer than the fast-time sampling interval, the term slow-time dimension is used accordingly. The integrated antenna architecture within a single modular form factor allows excellent SWaP features. Lastly, the antenna elements are represented by the spatial dimension that runs along the depth of the cube.

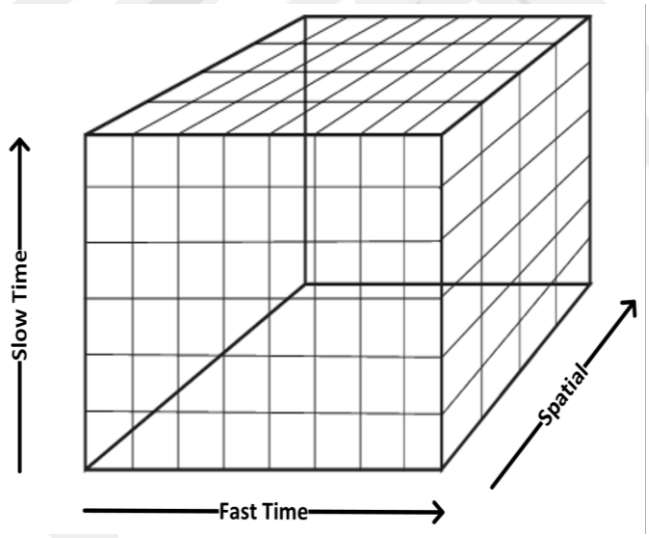

Figure 6.2 Typical Arrangement of a Radar Cube [77]

6.4. An Abridged Discussion on Windowing

Windowing is a technique applied to time-domain signals to avoid spectral leakage. It ensures that frequency analysis is done accurately [78]. The process entails the multiplication of the IF signal with entries of pre-programmed LUT in a DSP. This decreases spectral leakage and enhances frequency resolution. Rectangular and flat-top windows are not ideally suited for altimetry due to closely spaced beat frequencies. However, Hamming, Hanning, and Blackman windows are the favored choices

instead. Hamming window optimizes the trade-off between the width of the main lobe and the levels of the side lobes. Hanning window enhances the suppression of side lobes. Blackman window offers the most effective roll-off of side lobes and a wide main lobe. After careful consideration, the Blackman window was employed in this work before range-FFT, having no impact on CFAR peak grouping. The mathematical representation of the Blackman window in the time domain is given by

$$w(n) = 0.42 - 0.5\cos\left(\frac{2\pi n}{N-1}\right) + 0.08\cos\left(\frac{4\pi n}{N-1}\right), \quad (34)$$

where N is the number of ADC samples. During CFAR detection, the windowing method selection is crucial because of the faster roll-off rate of the Blackman window, which suppresses noise in neighboring range bins not containing the returns from the terrain. However, there is little value offered by windowing after the Doppler processing due to a limited number of receive antennae and coarse angular resolution.

6.5. Range-Doppler FFT Processing

The DFT of signals in the time domain is evaluated using the FFT, a powerful tool for spectral examination. Accurate range estimate in radar applications relies on breaking down the IF signal into beat frequencies present within. Each unique beat frequency provides information about the distance of the respective targets by measuring the TOF. The FFT step is mathematically given by

$$X(k) = \sum_{n=0}^{N-1} x(n) \cdot e^{-j2\pi kn/N}, \quad (35)$$

where N is the size of FFT, $X(k)$ is a set of beat frequencies present in the temporal IF signal, $x(n)$. The FFT process essentially puts the PSD against each beat frequency into its respective range bin. The range-FFT for multiple Doppler chirps can then be expressed as [79].

$$X(k,\tau) = \sum_{n=0}^{N_R-1} x(n,\tau) \cdot e^{-j2\pi kn/N_R}\ \tau = 0\ to\ N_D - 1, \quad (36)$$

where $X(k,\tau)$ is an extension of $X(k)$ with τ being the Doppler chirp index with k range bins. N_R and N_D are range and Doppler FFT sizes, respectively. The purpose of Doppler-FFT is to estimate the phase variations in beat frequencies caused by the relative motion of targets. Although slow time is crucial in many automotive applications, it is not significant in RA, as the objective is to estimate altitude rather than monitoring velocity. However, the relevance of Doppler calculation is argued in Chapter 7 in the context of Doppler correction, a critical concept associated with TDM-

MIMO for the resolution of phase uncertainty. The mathematical representation of the Doppler-FFT is provided as

$$Y(k,\tau) = \sum_{n=0}^{N_D-1} X(k,\tau) \cdot e^{-j2\pi kn/N_D},\ k = 0\ to\ N_R - 1, \qquad (37)$$

where $Y(k,\tau)$ is the output of the 2D-FFT stage for one antenna. 2D-FFT for numerous chirps per antenna per frame allows noncoherent integration to improve the SNR and achieve a reasonably low PFA. Improving SNR is extremely important in radar applications, especially within the context of mmWave automotive radars that have limited transmission power.

6.6. Detection Matrix

The generation of the detection matrix is a critical step before the CFAR stage. This process involves combining the 3D spatial data, which contains separate range-Doppler maps for each receiving antenna, into a single, integrated range-Doppler map. The selection of integration methodology is solely determined by the specific case being considered [36]. Coherent integration is a technique that combines numerous chirps in a way that enhances the power of the signal. This technique is used to improve the overall signal quality. Nevertheless, ensuring consistent phase relationships between successive chirps poses a significant challenge for a drone with significant mobility. Conversely, noncoherent integration is oblivious to phase considerations, which is better suited for mobile platforms. However, the improvement in SNR is not as significant as the coherent integration.

6.7. Foundation of AoA Estimation

The assessment of the direction of a signal at the radar with respect to its boresight is termed as the AoA. In legacy radar system with AoA capability necessitates the use of two or more Rx antennae and a single Tx antenna, termed as SIMO. To improve the accuracy of angular measurements, it is necessary to increase the quantity of Rx antennae. For example, SIMO radars with four and eight receive antennae can attain an angular resolution of 28.64° and 14.32° respectively. Figure 6.3 elucidates the concept of a SIMO radar with two Rx antennae having separation, d between them. The signal arrives at both Rx antennae making an angle, θ relative to the boresight. The signal travels an additional distance of $d\sin\theta$ for the Rx-2 antenna. The phase difference among the signals received at antennae is mathematically given by

$$\omega = \frac{2\pi}{\lambda} d sin\theta, \tag{38}$$

where λ and θ are the wavelength and angle, respectively. The expression $\frac{2\pi}{\lambda}$ is commonly referred to as the wavenumber. Therefore, by estimating the phase difference ω, the AoA can be evaluated as

$$\theta = \sin^{-1}\left(\frac{\omega\lambda}{2\pi d}\right). \tag{39}$$

For a maximum value of phase being, $|\pi|$, (39) can be maximized when d is $\frac{\lambda}{2}$. The result is the maximum limit of the FOV expressed as

$$\theta_{FOV} = \pm\frac{\pi}{2}. \tag{40}$$

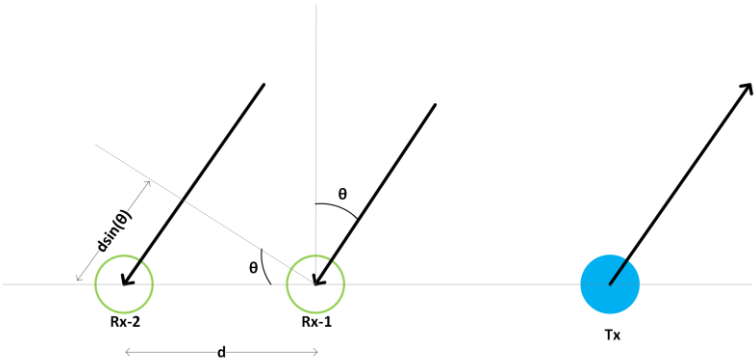

Figure 6.3 AoA Estimation in a SIMO Configuration [40].

As a rule, for any radar having N_{Rx} antennae, each ensuing antenna receives the reflected signal with an added phase difference of ω with respect to the prior, forming a continuing series [0 ω 2ω $\ldots N\omega$]. The periodic pattern can be approximated by employing a third stage of FFT, known as the angular FFT. The frequency components in this FFT resolve the targets into angular bins corresponding to their angular position with respect to the radar. When a target is perfectly aligned at the center, the reflected signals arrive at the antennae array at the same time. Subsequently, the object is resolved into the DC angular bin. Angular resolution can be mathematically expressed as

$$\theta_{RES} = \frac{2}{N_{Rx}}, \tag{41}$$

where θ_{RES} is the angular resolution in radians. N_{Rx} is the receiving antennae count. The mathematical inference of equation (41) is outside the scope of this investigation.

However, readers are motivated to consult reference [40] for a comprehensive explanation. Equation (41) indicates that it is possible to acquire a highly precise angular resolution by increasing N_{Rx}. Nevertheless, there are constraints in terms of volume, cost, and complexity. In Chapter 7, there is a detailed explanation of the notion of TDM-MIMO, which aims to address this difficulty by providing a suitable alternative. The purpose of the debate in this Chapter was to explicate the fundamentals of AoA in SIMO radars and pronounce the constraints associated with increasing the N_{Rx} before it becomes impractical from a realizability perspective.

CHAPTER 7

THE CRUISE STAGE

The cruise stage of an airborne platform refers to the phase of level flight that occurs after reaching the initial cruise altitude and continues until the descent to the destination begins. In the realm of UAS, this refers to the phase of flight during which a certain task is carried out. When it comes to applications that require the UAS to consistently maintain a specific altitude AGL, it is necessary to employ an RA. The primary objective of a RA, as previously stated, evaluation of AGL altitude at an update rate governed by the methodology cited in Chapter 5. The methodology comprised finding a compromise between maximum range and resolution against practical requirements to be encountered in the UAS flight operations. It has been already cited multiple times that that though Doppler evaluation is not a primary goal, the changes in aircraft altitude and terrain profile induce an unwanted effect [81]. Characterizing and remedying the impact of these effects on altitude estimates is of utmost importance. To achieve this objective, terrain models were obtained from MATLAB [82]. Figure 7.1 displays the variability in terrain elevation for different types of land.

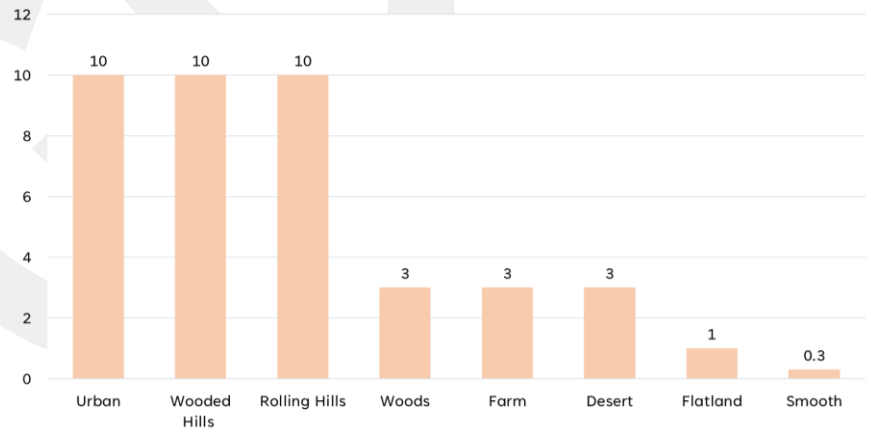

Figure 7.1 Elevation Represented as a Function of Standard Deviation [82]

Step size is the precise distance or gap between consecutive measurements, sensor readings, or location updates in a system. Within the framework of radar-based terrain sensing, the step size generally denotes the distance covered by the platform

carrying the radar between two successive radar scans or data points. This step size determines the level of detail and precision in the sensing process. Since the step size was not available, it was deemed suitable to consider it as the magnitude of horizontal displacement traversed in a second. Therefore, for a value of 20 m/s, there is a variation of 10 m in the terrain profile implying a 10 m/s radial velocity. The worst-case scenario is deliberately considered to address the most extreme possible situation. In a practical situation, the variation in altitude is likely to be much smaller. Table 7.1 lists the flight requirements of the cruise phase with the parameters for the resulting waveform summarized in Table 7.2.

Table 7.1 Requirements for Waveform Design in the Cruise Stage

Requirement	Value	Remarks
R_{acc}	±0.45 m	Range Accuracy
R_{min}	150 m	Minimum Range
R_{max}	300 m	Maximum Range
V_{lat}	20 m/s	Lateral Velocity
σ_h	10 m	Standard Deviation of Terrain
V_{rad}	10 m/s	Radial Velocity
SNR_{min}	20 dB	Minimum SNR Requirement
T	273.15 °K	Temperature in Degree Kelvin

Table 7.2 Waveform Parameters of RA in the Cruise Stage

Parameter	Value	Remarks
Δt_{max}	3.6653 s	Data Update Interval
U_{min}	0.2728 Hz	Lower Limit of Update Rate
T_c	1 ms	Chirp Time Period
B	1 GHz	Slope of FMCW Chirp
$\Delta R(B)$	0.15 m	Function of FMCW Chirp BW
IF_{max}	3 MHz	Maximum Beat Frequency
F_s	3.33 MSPS	ADC Sampling Rate
S	1 MHz/μs	FMCW Chirp Slope
N_{FFT}	4096	FFT Order
Δf	805.66 Hz	Frequency Resolution
$\Delta R(F_s, N_{FFT}, S)$	0.13 m	Function of FMCW Chirp Slope
N	16	FMCW Chirp Frame Size
T_F	16 ms	FMCW Chirp Frame Period
$V_{\max}$	0.974 m/s	Maximum Velocity
N_{Tx}	1	Number of Tx Antennae
N_{Rx}	4	Number of Rx Antennae
θ_{res}	28.64°	Angular Resolution
B_n	62.5 Hz	Noise BW

P_n	−141.27 dBm	Noise Power
σ_0	2.47	NRCS
$R_{max}(SNR_{min})$	4586 m	Function of SNR Requirement
$R_{max}(IF_{max}, S)$	450 m	Function of Maximum IF BW
$R_{max}(N_{FFT}, \Delta R)$	540 m	Function of FFT Order
Alt_{max}	450 m	Maximum Measurable Altitude

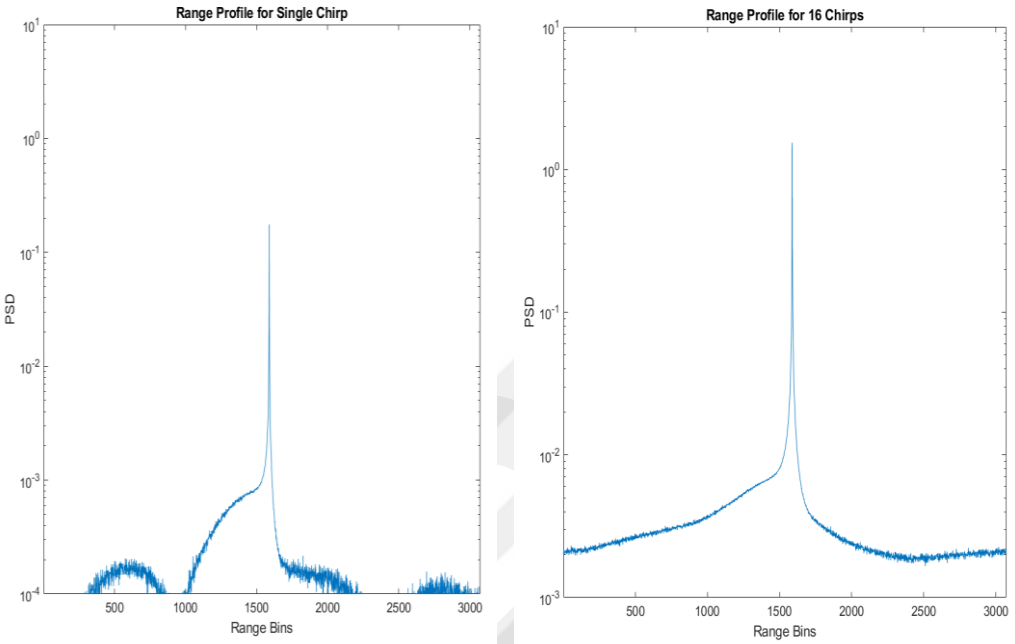

(**a**) (**b**)

Figure 7.2 Range Profile (a) Single chirp; (b) 16 chirps

The waveform design methodology in Chapter 5 also took these constraints into consideration. It was suggested that these restrictions also have an impact on how well RAs function in terms of signal processing. It was shown that a longer chirp length reduces noise BW and enables an IF filter with a significantly smaller BW to meet high-altitude requirements. To this end, a slower chirp slope can be employed. As a result, the maximum range can be set higher without sacrificing range resolution. This upper constraint, however, reduces the V_{max} to an extremely small value causing folding. The scenarios were simulated in the MATLAB environment. The simulation results yielded that the 0^{th} Doppler bin can be safely regarded as the range profile since the radial velocity contribution is only 10 m/s. With actual velocity components are bound to be much lower than the worst-case scenario considered in this investigation, the empirical approach fits in well with the scope of application.

As stated in preceding chapters, the intrinsic purpose of an RA is to estimate the altitude but to cater for the low Tx power by increasing the SNR in the detection stage, Doppler chirps are integrated non-coherently. This non-coherent integration is an inherent outcome of the 2D-FFT stage. Figure 7.2 shows a comparison of the 0^{th} Doppler bins signifying range profiles for an FMCW frame with a single chirp and 16 chirps with an evident increase in SNR .

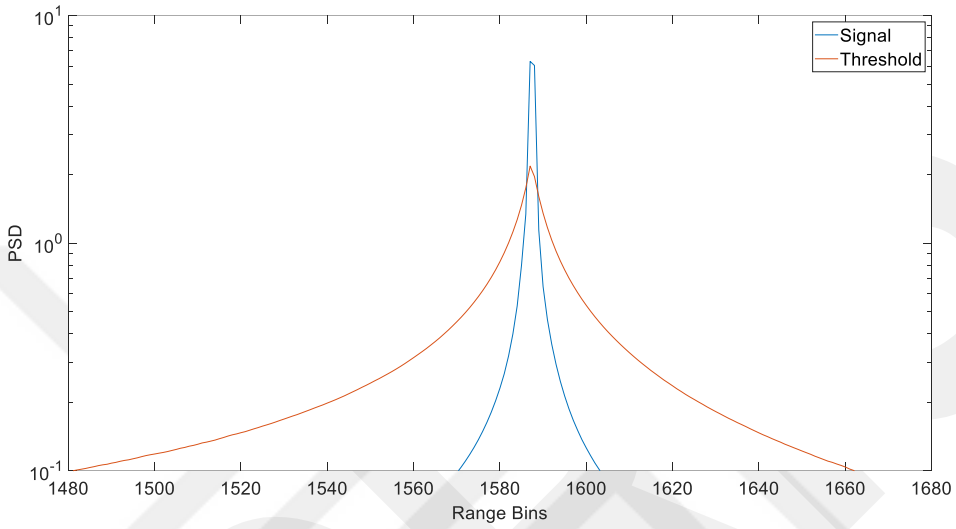

Figure 7.3 Range Profile and CFAR Threshold

However, a lengthy chirp has intrinsic restrictions of its own. The target is dispersed over several range bins due to the radial velocity component. In Figure 7.3, a relatively flat peak spanning over neighboring range bins is evident in the range profile. For a chirp duration of 1 m, there is a displacement of 1 cm for a radial velocity of 10 m/s. Per the requirement of update rate, the altitude information is shipped out of the radar at the end of each frame. Resultantly, a total of 16 cm distance is covered over the course of 16 chirps with a total frame period of 16 ms. Since each range bin has a width of 10 cm, the target transitions to the right or left range bins and spends 6 ms after spending 10 ms in the initial bin. The movement to neighboring bins is governed by the direction of relative motion. The drawback of a chirp with a slower slope is therefore at most a 10 cm degradation in range accuracy with the cumulative loss of 20 cm. Given a 45 cm range accuracy requirement, this trade-off is reasonable in return for an increased upper limit of maximum range.

7.1. CFAR for Terrain Detection

After obtaining the range profile, the succeeding task is the validation of peaks if they correspond to actual terrain. Based on considerable evidence in the literature, CFAR algorithm was chosen for this thesis. It automatically adjusts the detection threshold dynamically to maintain a consistent false alarm rate according to variations in noise levels. It is crucial to appraise the detection capability of CFAR in light of the fluctuating terrain elevation profile.

The CFAR algorithm has three primary versions, which are distinguished by the method used to determine the noise threshold. In CFAR-CA, the average noise levels from the cells on either side surrounding the target cell are used for evaluation of detection threshold. By utilizing the lowest and highest average noise levels, respectively, from the training cells next to the target cell on either side, the detection threshold is determined in CFAR-CASO and CFAR-CAGO. To prevent signal leakage in the process of estimating background noise, guard cells are employed. The guard cells are intentionally left out in the noise estimation process to ensure a more precise calculation. If N_T signifies the number of cells employed for noise calculation in CFAR-CA on one side, the detection threshold for cell, $N(k)$ is quantitatively expressed as

$$N_{CA} = \frac{1}{2N_T}\sum_{k=1}^{2N_T} N(k), \tag{42}$$

Although easy to implement on an actual DSP, it may not be as efficient in practical scenarios for terrains with considerable variations. The ensuing text reveals that CFAR-CASO is a better fit for terrains with high variations. Using (42), the mathematical equivalent for CFAR-CASO is given as [5]

$$N_L = \frac{1}{N_L}\sum_{k=1}^{N_L} N(k), \tag{43}$$

$$N_R = \frac{1}{N_R}\sum_{k=1}^{N_R} N(k). \tag{44}$$

The noise level is determined by selecting the smaller of the two averages as

$$N_{CASO} = \mathrm{Min}(N_L, N_R). \tag{45}$$

CFAR determines the detection threshold as a function of PFA [83] with scaling factor expressed as

$$\alpha = N_{CASO}\left(PFA^{-\frac{1}{N_{CASO}}} - 1\right). \tag{46}$$

It is clear from (46) that a low PFA value results in a greater scaling factor value. Aptly, the expression for threshold evaluation is given as

$$T(k) = \alpha \times N_{CASO}(k). \tag{47}$$

The output of CFAR is a binary matrix of size equal to number of range bins, N_{FFT} mathematically expressed as

$$V(k) = \begin{cases} 1, & V(k) > T(k) \\ 0, & otherwise \end{cases}, \; k = 0, 1, 2, 3 \ldots N_{FFT} \tag{48}$$

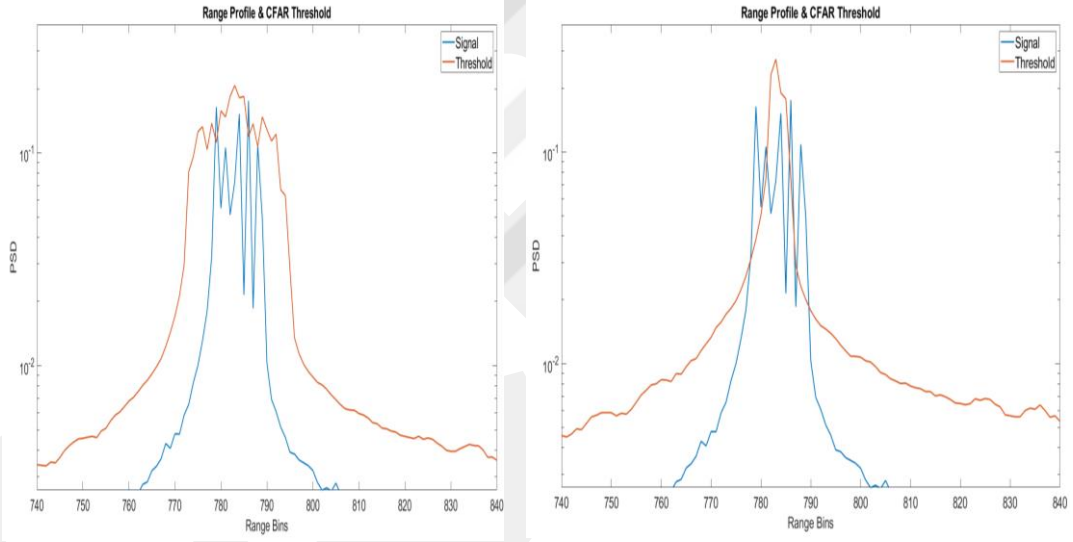

(**a**) (**b**)

Figure 7.4 CFAR threshold for: (a) CFAR−CA; (b) CFAR−CASO.

CFAR-CASO is used to validate prospective target with statistical significance. A side-by-side comparison is demonstrated in Figure 7.4 for CFAR-CA and CFAR-CASO. A rugged terrain has been simulated with five closely spaced patches. Despite a higher value of threshold for CFAR-CASO, it still remains capable of detecting a greater number of targets. This suggests a decrease in the PFA while still maintaining the ability to detect a greater number of targets with a more accurate estimation of background noise. Overall, whereas CFAR-CA offers a simple method for detecting targets, the CFAR-CASO comes out as the more superior option in managing terrain clutter having high variation. CFAR-CAGO has been deliberately glossed over owing

to limited performance in the current context. For the case of RA, altitude AGL is reported instead of the entire matrix, $V(k)$. Aptly, the terrain reflection with the highest PSD from the set of valid targets is the default choice. The breakout board of AWR1843 used in this investigation has a well-defined main lobe. Accordingly, it is anticipated that the terrain patch located at the boresight shall be reported as the altitude by virtue of having the highest PSD amongst valid targets [16]. The combination of peak grouping and the antenna characteristics are well aligned to enhance the accuracy of altitude estimation.

7.2. Efficacy of AoA Estimation using SIMO Radars at a High Altitude

Despite high altitude requirements in the cruise stage, the presence of multiple receive antennae in the radar platform may be exploited for AoA estimation. It may be categorically applicable in sifting returns from off-boresight targets leading to a more accurate altitude measurement. Nevertheless, multiple Rx antennae allow for non-coherent integration leading to an enhanced SNR, a desirable situation for estimating high-altitude.

Due to significant computational overhead, it is necessary to decide if the addition of AoA capability has a substantial benefit at high altitudes. Figure 7.5 exhibits a rudimentary concept of operation comprising a small VTOL drone hovering at 180 m AGL. Points A and B denote the crest and level terrain segments respectively. According to Table 7.1, 150 m is the lower limit of the altitude requirement hence the value of p has been taken as 180 m. Subsequently, the Pythagorean theorem is employed for the calculation of base length, Δd. For the radar to resolve A and B into distinct angular bins, θ and θ_{res} are taken as 28.64°. It is established that a separation, Δd, of approximately 98.3 m must be present between points A and B. It is therefore concluded that AoA estimation using a 1 × 4 SIMO configuration has very little gain. Nevertheless, the improvement in SNR via noncoherent integration is still relevant along the antenna dimension. Equation (37) provided a 2D range-Doppler map for one receive antenna. By extending (37) for multiple antennae, the SNR-enhanced equivalent typically termed the detection matrix is given by

$$D(k,\tau) = \sum_{a=1}^{N_{Rx}} |Y(k,\tau,a)|, \tag{49}$$

where $Y(k,\tau,a)$ is the extended version of (37) with the addition of the a signifying the antenna index and $|.|$ is the modulus operator. (49) holds more value from the perspective of CFAR detection owing to greater SNR. This increase in SNR is mathematically expressed as

$$P_{\text{int}} \approx N_{\text{Rx}} \cdot P_{\text{a}}, \tag{50}$$

where P_{int} and P_{a} indicate the magnitude of the signal strength prior to and following the integration step. Since the phase is not summed in a coherent manner, the gain increases by a factor of N_{Rx} only.

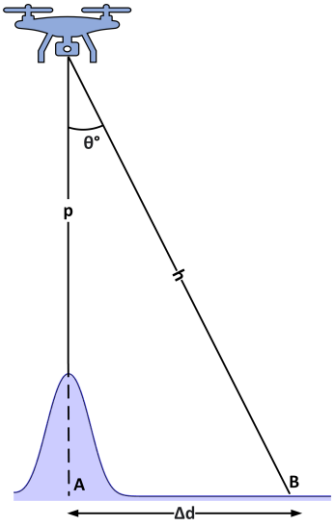

Figure 7.5 Simulated Scenario with a Single Crest and Level Terrain

CHAPTER 8

THE LANDING APPROACH STAGE

In the aviation industry, RAs are invaluable, especially when it comes to the landing approach phase making this the most important aspect of the thesis. The usefulness of employing TDM-MIMO for achieving high angular resolution is argued in this chapter. By capitalizing on the SWaP metrics of the chosen radar, the goal is to exploit high angular resolution to augment situational awareness in tough landing scenarios. The theoretical and quantitative aspects of TDM-MIMO coupled with the concept of virtual antennae are extensively debated. Two scenarios have been simulated comprising a small VTOL drone landing on a ship to appraise the practicality of TDM-MIMO.

8.1. Achieving High Angular Resolution with TDM-MIMO

The discussion on SIMO radar concluded with mathematical expressions that increasing the receive antennae count results in a finer angular resolution. However, physical antennae can only be increased to a certain limit. The limitation stems from the fact that adding antennae means not just paying more in volume, but the device requires discrete receiver chains. The superior SWaP properties of the automobile radars and their remarkably cheap production costs served as the foundation for this research endeavor. Accordingly, any direction that deviates from the said premise is beyond the context of this thesis. Appropriately, MIMO radars are an efficient means to double the θ_{RES} with a volumetric overhead of one extra emitter antenna with no additional burden in terms of the receiver chain as depicted in Figure 8.1.

In the discussion concerning SIMO radars, it was demonstrated that the spacing between the antennae, d is $\lambda/2$. When an FMCW signal is emitted from Tx1, a phase of $[0\ \omega\ 2\omega\ 3\omega]$ is produced at the four Rx antennae. A distance of $4d$ is strategically kept between Tx1 and Tx2 such that signal from Tx1 traverses an added $4dsin\theta$ distance with respect to Tx1. Consequently, the respective receive antennae also inherit an extra phase of 4ω being $[4\omega\ 5\omega\ 6\omega\ 7\omega]$. Eventually, a concatenated periodic sequence is formed as $[0\ \omega\ 2\omega\ 3\omega\ 4\omega\ 5\omega\ 6\omega\ 7\omega]$. It may be observed that

the said sequence is identical to 1 x 8 SIMO radar shown in Figure 8.2. The 2-Tx and 4-Rx antenna configuration effectively forms a virtual array with eight Rx antennae.

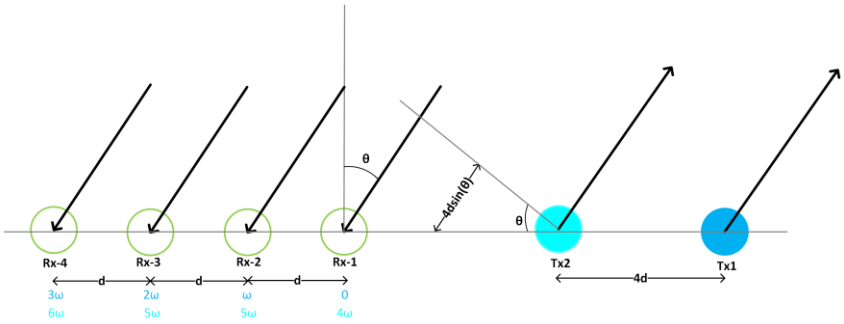

Figure 8.1 2Tx-4Rx TDM-MIMO Radar

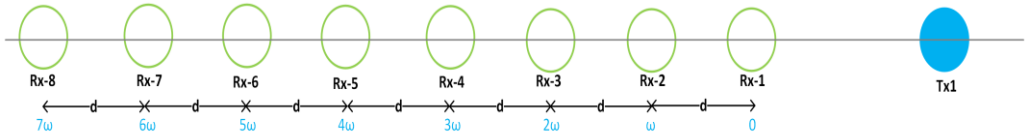

Figure 8.2 1Tx-8Rx SIMO *R*adar

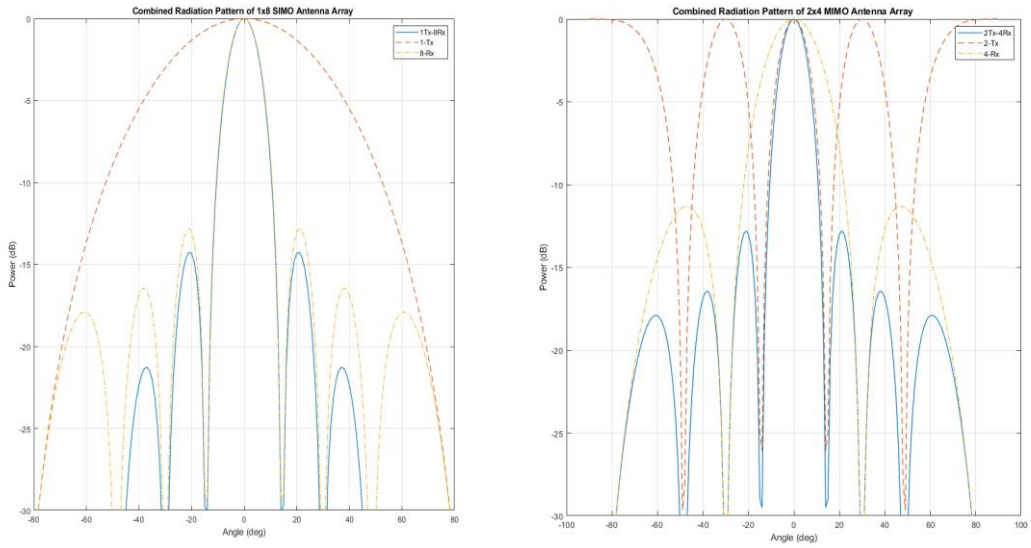

(a) (b)

Figure 8.3 Beam Pattern of (a) 1x8 SIMO (b) 2x4 MIMO

The angular resolution is improved as a result of this large increase in the virtual antennae count. Radiation patterns for SIMO and MIMO antenna designs are shown in Figure 8.3. It is clear that the aggregate beam width of the two designs is the same, yet MIMO only needs six antennae overall, whereas SIMO requires nine. This

significantly reduces the complexity and volume of the radar. The need for the radars to be able to separate and isolate the signals emanating from various Tx antennae cannot be overstated. TDM and BPM are two methods that are frequently used in the literature [26]. Owing to the relative ease of implementation, TDM-MIMO was preferred for this investigation instead of BPM-MIMO. Since these methods have not been well studied for mmWave RAs in UAS, TDM-MIMO was chosen as a suitable option for preliminary investigation. BPM-MIMO entails an additional increase in power budget of 3dB. But as MIMO is only used during the landing approach at low altitudes, this advantage is not very significant. Accordingly, due to the simple implementation of TDM-MIMO and same angular resolution, the choice to move forward with it was justified because the benefit associated BPM-MIMO is negligible. Table 8.1 lists the requirements of RA to be designed for the said flight stage.

Table 8.1 Requirement of RA for the Landing Approach

Requirement	**Value**	**Remarks**
R_{acc}	±0.45 m	Range Accuracy
R_{min}	5 m	Minimum Range
R_{max}	150 m	Maximum Range
V_{lat}	20 m/s	Lateral Velocity
RoD	5 m/s	Platform Rate of Descent
σ_h	2 m	Standard Deviation of Terrain
V_{rad}	7 m/s	Radial Velocity
SNR_{min}	20 dB	Minimum SNR Requirement
T	278.15 °C	Temperature in Degree Kelvin

The transmission for Tx antennae are temporally independent in TDM-MIMO. Figure 8.4 illustrates the arrangement of time slots for Tx antennae. To generate a detection matrix, the range-Doppler maps for every virtual antenna are noncoherently integrated using (49). Afterwards, valid targets are identified employing the CFAR-CASO detection from (48). As opposed to applying the angular FFT to every bin of the detection matrix, it may only be applied to the objects that the CFAR algorithm has identified as valid targets. This strategy enables a notable implementation optimization. The improved SNR from integration along the antenna dimension, which results in better CFAR detection performance, is the rationale behind the use of the detection matrix. Subsequently, it is essential to compensate for phase alteration induced by the rapid ROD of the UAS with respect to the terrain. As discussed in

Chapter 7, the 0[th] Doppler bin was empirically chosen as the range profile based on the specifics of the test case. In the next stage, CFAR-CASO detection is applied to $D(k,1)$ presented in (49).

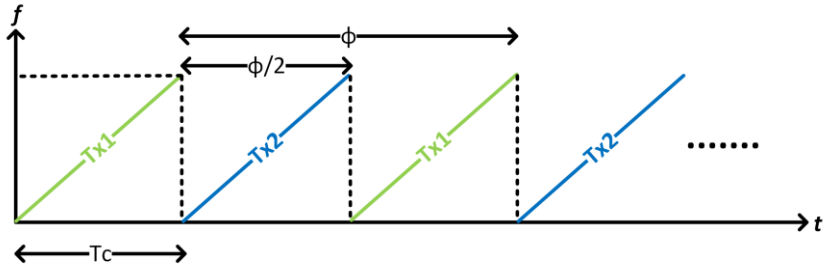

Figure 8.4 Doppler Induction due to UAS ROD in TDM-MIMO.

To evaluate the phase shift due to relative motion, the Doppler bin index, τ_i is evaluated as

$$\tau_i = arg\,\max_{\tau} D\,(k_i,\tau), \tau = 1,2,3 \ldots N_{Dopp}, \tag{51}$$

where $argmax$ function computes index of the bin containing maximum value. The phase difference as shown in Figure 8.4 may then be estimated as

$$\varphi = \frac{2\pi\tau_i}{N_{Dopp}}, -\frac{N_{Dopp}}{2} < \tau_i < \frac{N_{Dopp}}{2} - 1. \tag{52}$$

The rationale for phase compensation in TDM-MIMO that signal from Tx1 is concurrently received by the entire Rx antenna array. Therefore, the residual phase is attributed to the azimuthal location of the target in the antenna FOV. On the contrary, ambiguity arises in the phase difference detected between the two arrays of Rx antenna for Tx1 and Tx2. Accordingly, it cannot be ascertained whether the difference in phase is a consequence of motion, position, or a mix of both factors. The problem is significantly alleviated by the symmetric temporal arrangement of chirps in the FMCW frame devoid of any guard interval. The phase to be compensated may is quantitatively delineated as

$$\delta = \frac{\varphi}{2}, \tag{53}$$

The phase correction in (53) is required only for the virtual receive antennas associated with Tx2. Similar to the Doppler estimation step, phase compensation may be intelligently performed only on the bins containing valid targets. No correction is

necessary for virtual antennae numbered 1 to 4. The corrected range FFT for virtual antennae spanning from 5 to 8 is expressed as

$$\overline{X(k_i, \tau_i, v)} = X(k_i, \tau_i, v).\, e^{-j\delta}, \quad v = 5, \ldots, 8, \tag{54}$$

where $e^{-j\delta}$ is the phasor component signifying the compensation being performed. Equation (54) implies an unusual requirement that Doppler evaluation is warranted in a mmWave RA employing TDM-MIMO. The phase correction can only be performed once the phase is evaluated accurately in the first place deeming, $V_{\max}$ a serious limitation. For most small VTOL drones, the upper limit of ROD is approximately 5 m/s [84]. However, this study aims to propel mmWave RAs as a dynamic solution for a broad range of UAS types. Therefore, commercial UAS with fixed wings must be taken into consideration as well. An ROD of 1000 feet per minute (about 5 m/s) for a lightweight propeller aircraft was chosen based on comparable flight dynamics [85]. Since $V_{\max}$ is an essential element when TDM-MIMO is used for estimation of AoA, it the radial velocity component exceeds $V_{\max}$, Doppler-induced folding emerges as another limitation. As a resort, the chirp duration may be squeezed to accommodate a higher value of ROD. Chapter 9 entails possible workarounds for the cited challenge, to be investigated in future work. A summary of parameters for the mmWave RA waveform designed against the operational requirements of said stage is presented in Table 8.2.

Table 8.2 Waveform Parameters for mmWave RA in the Landing Approach Stage

Parameter	Value	Remarks
Δt_{max}	0.1223 s	Data Update Interval
U_{min}	8.14 Hz	Lower Limit of Update Rate
T_c	140 µs	Chirp Time Period
B	1 GHz	Slope of FMCW Chirp
$\Delta R(B)$	0.15 m	Function of FMCW Chirp BW
IF_{max}	10 MHz	Maximum Beat Frequency
F_s	12.5 MSPS	ADC Sampling Rate
S	7.1 MHz/µs	FMCW Chirp Slope
N_{FFT}	2048	FFT Order
Δf	6103 Hz	Frequency Resolution
$\Delta R(F_s, N_{FFT}, S)$	0.11 m	Function of FMCW Chirp Slope
N_{Dopp}	32	FMCW Chirp Frame Size
T_F	4.48 ms	FMCW Chirp Frame Period
N_{Tx}	2	Number of Tx Antennae
N_{Rx}	4	Number of Rx Antennae

θ_{res}	14.32°	Angular Resolution
B_n	223.21 Hz	Noise BW
P_n	-135.74 dBm	Noise Power
σ_0	2.47	NRCS
$R_{max}(SNR_{min})$	2426 m	Function of SNR Requirement
$R_{max}(IF_{max}, S)$	211 m	Function of Maximum IF BW
$R_{max}(N_{FFT}, \Delta R)$	264 m	Function of FFT Order
Alt_{max}	211 m	Maximum Measurable Altitude

8.2. TDM-MIMO for Enhanced Situational Awareness

This chapter builds upon the conceptual discourse and focuses on the application of mmWave RA capable of TDM-MIMO in the safety of UAS. A situation simulated comprising the landing of a small VTOL drone onto the concrete deck of a ship in a water body is investigated. Points A and B, separated by Δd, denoting the scattering area for the sea surface and the concrete deck of the ship, respectively are depicted in Figure 8.5. Table 8.3 contains the specifics of the two corner cases simulated for the scenario illustrated in Figure 8.5. All the lengths and angles are in meters and degrees respectively. The θ_{res} for the 2Tx-4Rx MIMO configuration comes out to be 14.32°. For the first simulation, θ is equal to θ_{res} with the rationale to resolve the returns from A and B in range as well as angular domain. For the second case, B is placed at a high off-boresight position and A is aligned straight under the drone. At an altitude of 4.67 m the θ being 57.28° moves B to a range of 8.63 m. Before delving further, it is crucial to realize the RCS variation between the concrete deck and the sea clutter. Deducing seas clutter models is a difficult undertaking in its own right. The task becomes even more daunting in the mmWave regime. Clutter modeling was discussed in Chapter 4 with reasonable quantitative and conceptual breakdown. Accordingly, it was deemed appropriate to refer to reputable literature on marine clutter. The MathWorks *seareflectivity* model comes equipped with reliable models to choose from according to the frequency range and grazing angle, ψ. After careful consideration, the TSC empirical model was chosen for the NRCS calculation of point A [86]. For point B, the findings from Chapter 4 are applicable since it is a concrete surface [63]. The scale factor of the sea surface determines its reflectivity. In other words, the greater the wind and tide, the higher the NRCS.

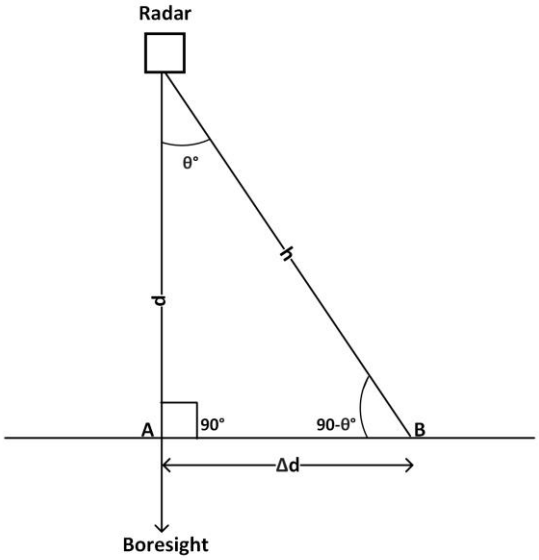

Figure 8.5 Landing Approach of VTOL UAS on a Ship

Table 8.3 Parameters for Figure 8.5

p	h	Δd	$\theta°$	**Remarks**
4.67	4.82	1.19	14.32	A and B are located in Adjacent Range bins
4.67	8.63	7.26	57.28	B located at Maximum Off-Boresight Angle

It is essential to accurately simulate real-world conditions that will contribute to a higher NRCS of point B causing difficulty to distinguish between the concrete deck and sea surface. However, a very large scale factor signifying a sea storm would make it impossible for a small-sized VTOL drone to fly, let alone land safely. Accordingly, a moderate value was empirically chosen. Secondly, positioning point B at a high offset angle decreases $\psi°$ culminating into a smaller NRCS. It must be remembered that the $\psi°$ is the 90° complement of θ. The mathematical equations associated with clutter modeling were purposefully omitted to restrict the discussion to the application. For a comprehensive understanding, readers are urged to consult the specified references [62], [64] − [86]. The reference manual of the AWR1843BOOST breakout board was consulted for antenna specifications [18]. Table 8.4 lists the specifications and resulting RCS values for each scenario.

The investigation demonstrates that despite point A having a larger $\psi°$ and being at a shorter range, its RCS remains minuscule compared to point B for each simulation. Nevertheless, the RCS of the concrete deck reduces manifolds in the second simulation owing to its smaller $\psi°$. Owing to a very small RCS, the CFAR detection does not identify point A as a valid target in both simulations. The residual task that is reporting

the strongest PSD in the range as the concrete deck and applying angular FFT to find the AoA as shown in Figure 8.6 for both simulations. In summary, without TDM-MIMO offering a very fine angular resolution, the RA would report point B at the radar boresight as the altitude with no AoA information. However, with the availability of AoA, it can be ascertained that the concrete deck indeed does not lie under the body of the drone but at an off-boresight position. This augments the situational awareness of UAS for landing in tough situations.

Table 8.4 Comparison of RCS

Specifications	**A**	**B Simulation 1**	**B Simulation 2**
Range (m)	4.67	4.82	8.63
θ_e	28°		
θ_a	56°		
Sea State	5	-	-
ψ	90°	75.68°	32.72°
Clutter Model	TSC	APL	APL
NRCS	0.008	20.35	0.9506
RCS (m^2)	0.052	135.49	11.34

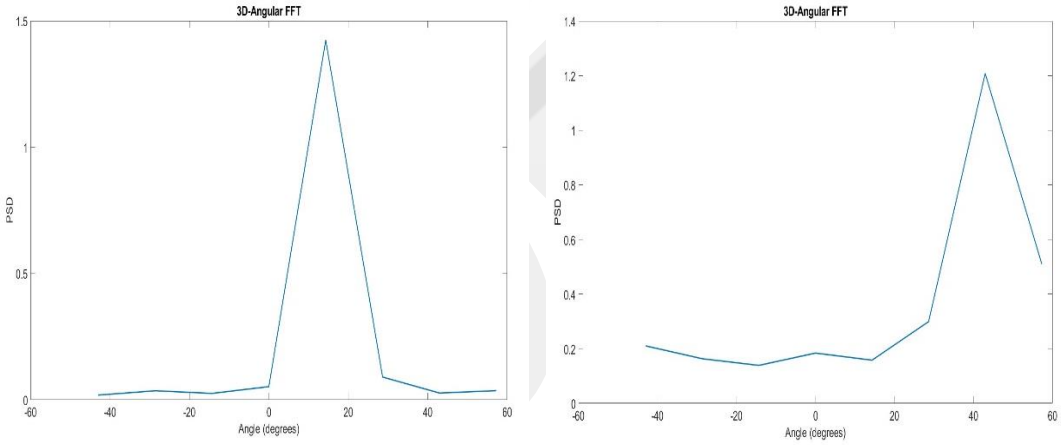

Figure 8.6 Angular FFT: (a) Simulation 1 (b) Simulation 2.

CHAPTER 9

AUTHOR'S DISCUSSION

The aim of this investigation was to propose an alternative avenue for RAs to migrate in the context of spectrum contention between contemporary RAs used in commercial aviation and 5G cellular networks. It was argued in the manuscript that automotive radars are a feasible candidate for resolving the problem at hand owing to their cost-effectiveness, software-defined architecture for waveform design, and SWaP metrics. However, there is a gap in the academic literature to study the inherent hardware constraints and propose a systematic methodology for optimal waveform design. However, it is important to underscore that by removing the bottlenecks of hardware specifications, the performance metrics can be improved even further. For instance, $R_{max}(IF_{max}, S)$ being a function of IF_{max} governs the Alt_{max}. It is important to understand that migrating to the mmWave regime, particularly 77 GHz has instrinsic benefits that are not limited to automobile radars. The findings of this thesis are applicable for waveform design in modular radars as well while for a higher value of IF_{max}. However, it comes at a cost of increased requirement of F_s which in turn nccessitates a higher order of N_{FFT}. Although DSP resources are limited on automotive radars, it is not a substantial challenge if a DSP is to be used externally to the MMIC. Nevertheless, modular radars do not have excellent SWaP features and are expected to be pricey rendering them unsuitable for inexpensive small VTOL drones. It was apprised in Chapter 4 that a shorter wavelength in the mmWave regime is an impediment to achieving a high SNR due to high FSPL. The investigation yielded that higher NRCS of terrain due to lesser penetration of shorter wavelengths provided a decent trade-off. Moreover, wide antenna projection and a longer frame period resulted in a very high $R_{max}(SNR_{min})$. In conclusion, regardless of the hardware used, the contribution of this thesis are poised to serve as a cornerstone for mmWave RAs in UAS. The lack of designated MOPS for UAS altimetry necessitated considerable deliberation on repurposing existing commercial aviation standards for use in UAS. The intertwined nature of performance metrics necessitated a meticulous approach.

Therefore, great care was exercised in devising a step-wise systems engineering approach. A test case was considered to elucidate the methodology of deriving waveform specifications from operational requirements.

After laying the groundwork for waveform design, the next step forward was orchestrating a framework for signal processing. Similar to the waveform design stage, hardware limitations necessitate that performance metrics be prioritized based on their role according to the flight stage. The software-defined architecture proved extremely useful in devising an adaptive waveform for the mmWave RA.

Equally relevant in theoretical basis, the interconnected nature of performance metrics is applicable in the signal processing stage as well requiring a careful approach. For instance, increasing the chirp duration is a compromise to be made for increasing the maximum range. It was observed that the terrain profile and UAS ROD had no major while the aircraft was cruising but the reflection from the terrain shifted to adjacent bins. Despite the radial velocity component caused by terrain fluctuations and a long-duration chirp, the range accuracy remained within the operational requirements. Although the effect was miniscule was miniscule, increasing the chirp period beyond a certain threshold will lead to a major degradation of range accuracy.

This work made a novel addition by offering TDM-MIMO owing to the benefit in terms of SWaP while offering fine angular resolution to increase situational awareness in UAS. There are, however, further explorations that will be undertaken in the interest of time as part of the ongoing project. Moreover, there are associated challenges that need to be addressed to maximize the fruit of this research endeavor.

9.1 Future Work

After thoroughly discussing mmWave altimetry for UAS, including supporting arguments, mathematical examples, and insights, it is necessary to set the course for future work. The scope of this effort must extend to experimental verification on different terrain types likely to be encountered in the flight of UAS including but not limited to vegetation, water, ice, and concrete. Experimentation is crucial for both validating the theoretical findings of this study and assessing the efficacy of the signal-processing strategies mentioned in this research. To fulfill this need, a two-step process is proposed. The first step involves the use of DTED of a real-world runway and simulating the UAS flight to gauge the increase in altitude accuracy gained from using a TDM-MIMO capable mmWave RA against a conventional counterpart. In this

thesis, uniform targets were simulated the propagation model did not account for reflections. To accurately replicate a real-world situation, it is crucial to consider the impact of specular reflections as well. Eventually, it is planned that radar shall be mounted on a small VTOL drone to emulate the cruise and landing approach phases of the UAS flight examined in this research. Consequently, there is disruptive potential to enhance landing safety in UAS operations and ensure consistent altitude in surveillance tasks. Optimization of performance metrics exhibited excellent outcomes in simulation and considering the increasing use of UAS in various aspects of modern life, it is necessary to propel the discourse in academia and industry towards MOPS specifically designed for mmWave altimetry in UAS.

ML/DL techniques have been extensively used in automotive radar applications. Surveys [8], [87] – [88] summarized the extraordinary work being done in this area. Particularly, their potential in the UAS domain is explored in a dedicated survey [89]. Based on the significant progress in this area, their application has the potential to benefit UAS altimetry as well. For instance, DL algorithms can be used to detect unwanted EM interference from other sources. Moreover, they can be leveraged for the classification of terrain types to dynamically adjust the waveform parameters.

9.2 Challenges

There are impediments to the practical deployment of mmWave automotive radars on UAS. For instance, a radome is mandatory to shield the avionics from environmental stress because the antenna array is housed on the same PCB. Design and manufacturing of a radome in the mmWave regime is likely to be a very expensive process. An alternative approach could be the use of horn antennae to house the avionics in an enclosure. However, the precise calibration during the mounting stage at mmWave frequencies is overkill for inexpensive small VTOL drones. The challenge will be further aggravated for the TDM-MIMO case since it implies an array of antennae. The calibration requirements position conformal antennae designed on the microstrip technology as a practical solution. However, the bending of substrates according to the UAS airframe is yet another inhibition. Additionally, there is a need to explore cheap substrates with low loss tangent and very low Young's Modulus at the same time [90]. No matter which antenna design is preferred, characterization is a substantial overhead at such high frequencies. Legacy techniques involving Faradic cages are very expensive. It is proposed that the radar may be used as a testbench to

estimate SNR against a target with known RCS at a pre-determined range. The evaluation software will come in handy for the realization of the proposed testing methodology [91]. Nonetheless, the characterization of emission pattern remains a challenging research endeavor in its own right for HPBW calculation.

There is a general lack of academic evidence apropos the long-term reliability of automotive radars when used in aerial deployments. Automotive-grade MMICs fare well at high temperatures against the high vibrational profile of automobiles. However, the vibration spectrum of UAS is an uncharted area warranting accelerated testing.

There are some intrinsic barriers to pursuing future objectives within the scope of signal processing despite encouraging simulation results. Firstly, actual hardware must be used to execute the simulation scenarios covered in this study. The implementation of waveforms for both flight stages is necessary. It is mandatory to document the implementation details as well as the characterization of processing latency that eventually governs the update rate. Furthermore, the engineering design of the hysteresis loop presents another formidable challenge. It must be ensured that there is a smooth transition of waveform between flight stages at the border of altitude limits [92]. Data-driven approaches can be leveraged to conveniently resolve the hysteresis loop challenge, but a more in-depth investigation is obligatory.

Making sure that abnormal limits and failures are always well accounted for is a key objective in the field of systems engineering. Drones surpassing the maximum ROD limit during the landing approach phase is one specific case that needs to be carefully considered. In the event of ROD being superseded, Doppler compensation will not be carried out appropriately, leading to incorrect estimation of AoA. This situation could have disastrous consequences for a safety-critical emergency landing scenario in UAS relying only on RAs. In safety-critical situations, there is no tolerance for inaccurate readings. It is essential to either provide precise reports with a high level of confidence or withhold reporting altogether when confidence is low. An alternative approach is to increase the $V_{\max}$ and use techniques to resolve the velocity ambiguity [32]. Extending the $V_{\max}$, however, has its limitations within the current scope, and it is still possible for the $V_{\max}$ to surpass a certain value of ROD. A comprehensive solution coupled with detailed inquiry is required in this situation.

CHAPTER 10

CONCLUSION

In response to the emerging 5G interference with legacy RAs, this thesis explores the use of mmWave automotive radars based on FMCW waveform for altitude measurement in UAS. A historical overview of contemporary RAs, frequency regulations, and choosing the optimal radar provide context, alongside discussions on performance metrics for a broad audience. A discourse on the estimation of clutter from terrain using specifications of AWR1843 was provided. Moreover, commercial aviation MOPS for RAs are assessed for potential adaptation to UAS altimetry, in the absence of dedicated standards.

Furthermore, this thesis presents a signal processing framework that addresses UAS altimetry across three two flight phases: cruise, and landing approach. Notably, the use of TDM-MIMO for enhanced situation awareness during the landing approach was largely unexplored. The discussion covers waveform design aimed at optimizing performance metrics, particularly maximizing altitude during the cruise and improving angular resolution during the landing approach stage.

Theoretical, mathematical, and practical insights were provided as guidance for a better understanding of radar signal processing, including chirp integration, range-Doppler mapping, and windowing techniques. FMCW radar scenarios were simulated for each flight stage where the CFAR-CASO algorithm provided a balanced solution for detecting terrain.

In conclusion, the research underscores the potential of mmWave altimetry while acknowledging future challenges and offering a course for future research. The groundwork laid here opens up new possibilities for enhancing UAS flight safety and performance and positions mmWave altimetry as a key area of focus moving forward.

CHAPTER 11

DELIVERABLES

The research presented in this thesis builds upon the foundational work detailed in references [93] and [94], both of which have been published during this study. These publications provide a comprehensive analysis of key aspects covered in the thesis and serve as important resources for understanding the methodologies and outcomes in greater depth. Readers who wish to explore the technical details, underlying frameworks, or extended discussions are strongly encouraged to consult these references. The publications offer additional insights that complement the findings presented here, contributing to a more thorough appreciation of the subject matter.

REFERENCES

[1] X. Zhang, Z. He, Z. Ma, P. Jun, and K. Yang, "VIAE-Net: An End-to-End Altitude Estimation through Monocular Vision and Inertial Feature Fusion Neural Networks for UAV Autonomous Landing," *Sensors*, vol. 21, no. 18, p. 6302, 2021.

[2] D. Gebre-Egziabher, R. C. Hayward, and J. D. Powell, "A Low-Cost GPS/Inertial Attitude Heading Reference System (AHRS) for General Aviation Applications," in *Proc. IEEE Position Location and Navigation Symposium*, 1998, pp. 518–525.

[3] S. Royo and M. Ballesta-Garcia, "An Overview of Lidar Imaging Systems for Autonomous Vehicles," *Applied Sciences*, vol. 9, no. 19, p. 4093, 2019.

[4] D. K. A. Pulutan and J. S. Marciano, "Design Trade-Offs in a Combined FMCW and Pulse Doppler Radar Front-End," in *Proc. IEEE Tencon Spring*, 2013, pp. 567–571.

[5] M. A. Richards, J. A. Scheer, and W. A. Holm, Eds., *Principles of Modern Radar: Basic Principles*, London, U.K.: Institution of Engineering and Technology, 2010.

[6] A. F. Tong, W. M. Lim, C. B. Sia, X. Yu, W. Yang, and K. S. Yeo, "Scalable RFCMOS Model for 90 Nm Technology," *International Journal of Microwave Science and Technology*, vol. 2011, pp. 1–16, 2011.

[7] V. Srinivasan, "CMOS MMIC Ready for Road, A Technology Overview," Texas Instruments, Feb. 2018. Available: https://www.ti.com/lit/an/swra592/swra592.pdf. [Accessed: Feb. 1, 2024].

[8] A. Soumya, C. K. Mohan, and L. R. Cenkeramaddi, "Recent Advances in mmWave-Radar-Based Sensing, Its Applications, and Machine Learning Techniques: A Review," *Sensors*, vol. 23, no. 21, p. 8901, 2023.

[9] C. Pichavant, "Use of 4200–4400 MHz Radio Altimeter Band," in *Proc. 24th Meeting of Working Group F Aeronautical Communications Panel*, Mar. 2011.

[10] J. Taylor, "Handbook on Radio Frequency Spectrum Requirements for Civil Aviation Part I," in *Proc. 28th Meeting of Working Group F Aeronautical Communications Panel*, Mar. 11–22, 2013.

[11] "LR-D1 Pro: Dual-Band Radar Altimeter," AINstein. Available: https://ainstein.ai/lr-d1-pro-dual-band-radar-altimeter/. [Accessed: Jun. 7, 2024].

[12] "Honeywell ALA-52B Radio Altimeter," Honeywell Aerospace. Available: https://aerospace.honeywell.com/us/en/products-and-services/product/hardware-and-systems/navigation-and-radios/ala-52b-radar-altimeter. [Accessed: Jun. 22, 2024].

[13] "Drone Technology in Agriculture," Croptracker. Available: https://www.croptracker.com/blog/drone-technology-in-agriculture.html. [Accessed: Jun. 16, 2024].

[14] K. Finklea, "Law Enforcement and Technology: Use of Unmanned Aircraft Systems," *Congressional Research Service*, June 2024. Available: https://crsreports.congress.gov/product/pdf/R/R47660. [Accessed: Jun. 15, 2024].

[15] D. D. Nguyen, J. Rohacs, and D. Rohacs, "Autonomous Flight Trajectory Control System for Drones in Smart City Traffic Management," *ISPRS International Journal of Geo-Information*, vol. 10, no. 5, p. 338, 2021.

[16] J.-S. Ha and S.-Y. Hong, "Altimetry Method for an Interferometric Radar Altimeter Based on a Phase Quality Evaluation," *Sensors*, vol. 23, no. 23, p. 5508, 2023.

[17] "MathWorks Radar Toolbox," MathWorks. Available: https://www.mathworks.com/help/radar/. [Accessed: Mar. 24, 2024].

[18] "Texas Instruments AWR1843BOOST Evaluation Module for Single Chip 77 GHz mmWave Sensor," Texas Instruments. Available: https://www.ti.com/tool/AWR1843BOOST. [Accessed: Apr. 14, 2024].

[19] Y. Zhang, Y. Qiao, G. Li, W. Li, and Q. Tian, "Random Time Division Multiplexing Based MIMO Radar Processing with Tensor Completion Approach," *Sensors*, vol. 23, no. 10, p. 4756, 2023.

[20] "MathWorks Radar Data Cube," MathWorks. Available: https://www.mathworks.com/help/phased/gs/radar-data-cube.html. [Accessed: May 11, 2024].

[21] S. Frick, "Radar Altimeters: Overview of Operation, Design, and Performance," *AVSI*. Available: https://avsi.aero/wp-content/uploads/2021/12/Radar-Altimeter-Overview-of-Design-and-Performance.pdf. [Accessed: Apr. 19, 2024].

[22] L. Cai, X. Ma, Q. Xu, B. Li, and S. Ren, "Performance Analysis of Some New CFAR Detectors under Clutter," *Journal of Computers*, vol. 6, no. 12, pp. 1278–1285, 2011.

[23] J. Scholvin, D. R. Greenberg, and J. A. del Alamo, "Fundamental Power, and Frequency Limits of Deeply Scaled CMOS for RF Power Applications," in *Proc. International Electron Devices Meeting*, San Francisco, CA, USA, Dec. 11–13, 2006.

[24] C. Pichavant, "Key Potential Operational Effects from 5G on Radio Altimeter," in *Regional Preparations for WRC 23 ATU*. Available: http://tinyurl.com/4awfamc2. [Accessed: Feb. 2, 2024].

[25] "FCC 47 CFR 15.249 Operation within the Bands 902–928 MHz, 2400–2483.5 MHz, 5725–5875 MHz, and 24.0–24.25 GHz," U.S. Government Printing Office. Available: https://www.govinfo.gov/content/pkg/CFR-2009-title47-vol1/pdf/CFR-2009-title47-vol1-sec15-249.pdf. [Accessed: Feb. 3, 2024].

[26] K. Ramasubramanian, K. Ramaiah, and A. Aginskiy, "Moving from Legacy 24 GHz to State-of-the-Art 77 GHz Radar," Texas Instruments, Oct. 2017. Available: https://www.ti.com/lit/wp/spry312/spry312.pdf. [Accessed: Feb. 1, 2024].

[27] J. Proakis, *Digital Communications*, New York, NY, USA: McGraw-Hill, 2001.

[28] M. Jankiraman, *FMCW Radar Design*, Norwood, MA, USA: Artech House, 2018.

[29] J. Hasch, E. Topak, R. Schnabel, T. Zwick, R. Weigel, and C. Waldschmidt, "Millimeter-Wave Technology for Automotive Radar Sensors in the 77 GHz Frequency Band," *IEEE Transactions on Microwave Theory and Techniques*, vol. 60, no. 4, pp. 845–860, 2012.

[30] W. Menzel and A. Moebius, "Antenna Concepts for Millimeter-Wave Automotive Radar Sensors," *Proceedings of the IEEE*, vol. 100, no. 7, pp. 2372–2379, 2012.

[31] Texas Instruments, "IWR1843, Single-chip 76-GHz to 81-GHz Industrial Radar Sensor Integrating DSP, MCU, and Radar Accelerator," Available: https://www.ti.com/product/IWR1843. [Accessed: Jan. 31, 2024].

[32] B. Ahmed, "Exploring the Potentials of Commercial Radar Chipsets for Proximity Sensing with Resolving Velocity Ambiguity," Ph.D. dissertation, Atilim Univ., Ankara, Turkey, 2022.

[33] B. Ahmed, A. Kara, E. Zencir, and M. Benzaghta, "Opportunities and Challenges in Measurement of 9-mm Bullet Model with 77 GHz mmWave COTS Radar Systems," Microw. Opt. Technol. Lett., vol. 62, no. 12, pp. 3772–3778, 2020.

[34] M. Alizadeh, "Remote Vital Signs Monitoring Using a mm-Wave FMCW Radar," M.S. thesis, Univ. Waterloo, Ontario, Canada, 2019.

[35] M. I. Skolnik, *Radar Handbook*, 3rd ed. New York, NY, USA: McGraw-Hill, 2008.

[36] B. R. Mahafza, *Radar Systems Analysis and Design Using MATLAB*, 3rd ed. Boca Raton, FL, USA: CRC Press, 2013.

[37] I. Bilik, O. Longman, S. Villeval, and J. Tabrikian, "The Rise of Radar for Autonomous Vehicles: Signal Processing Solutions and Future Research Directions," IEEE Signal Process. Mag., vol. 36, no. 3, pp. 20–31, 2019.

[38] S. M. Patole, M. Torlak, D. Wang, and M. Ali, "Automotive Radars: A Review of Signal Processing Techniques," IEEE Signal Process. Mag., vol. 34, no. 5, pp. 22–35, 2017.

[39] G. Hakobyan and B. Yang, "High-Performance Automotive Radar: A Review of Signal Processing Algorithms and Modulation Schemes," IEEE Signal Process. Mag., vol. 36, no. 4, pp. 32–44, 2019.

[40] S. Rao, "MIMO Radar," Texas Instruments, Dallas, TX, USA, Appl. Rep. SWRA554A, Jul. 2018. Available: https://www.ti.com/lit/an/swra554a/swra554a.pdf. [Accessed: Feb. 3, 2024].

[41] S. Rao, "Introduction to mmWave Sensing: FMCW Radars," Available: https://www.ti.com/content/dam/videos/external-videos/2/3816841626001/5415528961001.mp4/subassets/mmwaveSensing-FMCW-offlineviewing_0.pdf. [Accessed: Jan. 26, 2024].

[42] V. Dham, "Programming Chirp Parameters in TI Radar Devices," Texas Instruments, Dallas, TX, USA, Appl. Rep. SWRA553A, Feb. 2020. Available: https://www.ti.com/lit/an/swra553a/swra553a.pdf. [Accessed: Feb. 4, 2024].

[43] X. Li, X. Wang, Q. Yang, and S. Fu, "Signal Processing for TDM MIMO FMCW Millimetre-Wave Radar Sensors," IEEE Access, vol. 9, pp. 167959–167971, 2021.

[44] N. Wessendorp, R. Dinaux, J. Dupeyroux, and G. C. H. E. de Croon, "Obstacle Avoidance Onboard MAVs Using an FMCW Radar," in *Proc. 2021 IEEE/RSJ Int. Conf. Intelligent Robots and Systems (IROS)*, Sep. 2021, pp. 117–122.

[45] E. Sie, Z. Liu, and D. Vasisht, "BatMobility: Towards Flying Without Seeing for Autonomous Drones," in *Proc. 29th Annu. Int. Conf. Mobile Computing and Networking*, ACM, Oct. 2023, pp. 1–16.

[46] A. Safa, T. Verbelen, O. Catal, T. Van de Maele, M. Hartmann, B. Dhoedt, and A. Bourdoux, "FMCW Radar Sensing for Indoor Drones Using Learned Representations," 2023.

[47] P. Hugler, M. Geiger, and C. Waldschmidt, "77 GHz Radar-Based Altimeter for Unmanned Aerial Vehicles," in *Proc. 2018 IEEE Radio and Wireless Symp. (RWS)*, Anaheim, CA, USA, Jan. 2018, pp. 129–132.

[48] P. Hugler, F. Roos, M. Schartel, M. Geiger, and C. Waldschmidt, "Radar Taking Off: New Capabilities for UAVs," IEEE Microw. Mag., vol. 19, no. 4, pp. 43–53, 2018.

[49] Ö. O. Başpınar, B. Omuz, and A. Öncü, "Detection of the Altitude and On-the-Ground Objects Using 77-GHz FMCW Radar Onboard Small Drones," Drones, vol. 7, no. 2, pp. 86, 2023.

[50] EUROCAE, *Minimum Performance Specification for Airborne Low Range Radio Altimeter Equipment*, ED-30, Mar. 1980.

[51] RTCA, *Minimum Performance Standard for Airborne Low-Range Radar Altimeters*, DO-155, Nov. 1974.

[52] J.-S. Ha and S.-Y. Hong, "*Altimetry Method for an Interferometric Radar Altimeter Based on a Phase Quality Evaluation*," Sensors, vol. 23, no. 23, p. 5508, 2023.

[53] F. C. Robey, S. Coutts, D. Weikle, J. C. McHarg, and K. Cuomo, "MIMO Radar Theory and Experimental Results," in *Proc. 38th Asilomar Conf. Signals, Systems and Computers*, Pacific Grove, CA, USA, Nov. 2004, pp. 300–304.

[54] H. Rohling and R. Mende, "OS CFAR Performance in a 77 GHz Radar Sensor for Car Application," in *Proc. Int. Radar Conf.*, Beijing, China, Oct. 1996, pp. 109–114.

[55] P. Hugler, M. Geiger, and C. Waldschmidt, "77 GHz Radar-Based Altimeter for Unmanned Aerial Vehicles," in *Proc. 2018 IEEE Radio and Wireless Symp. (RWS)*, Anaheim, CA, USA, Jan. 2018, pp. 129–132.

[56] P. Hugler, F. Roos, M. Schartel, M. Geiger, and C. Waldschmidt, "*Radar Taking Off: New Capabilities for UAVs*," IEEE Microw. Mag., vol. 19, no. 4, pp. 43–53, 2018.

[57] J. Ma, J. Xiang, and F. Peng, "*Performance Analysis of CFAR Detector Based on Censored Mean and Cell Average*," J. Phys. Conf. Ser., vol. 1237, no. 1, p. 022029, 2019.

[58] N. Sakhuja, *MMWAVE-SDK Deep Dive*, Texas Instruments, Dallas, TX, USA, 2020.

[59] MathWorks, "Phased Array System Toolbox," Available: https://www.mathworks.com/help/phased. [Accessed: May 15, 2024].

[60] J. Park, H. Ryu, K.-W. Ha, J.-G. Kim, and D. Baek, "*76–81-GHz CMOS Transmitter with a Phase-Locked-Loop-Based Multichirp Modulator for Automotive Radar*," IEEE Trans. Microw. Theory Tech., vol. 63, no. 5, pp. 1399–1408, 2015.

[61] A. V. Oppenheim, A. S. Willsky, and S. H. Nawab, *Signals & Systems*, Prentice-Hall, Upper Saddle River, NJ, USA, 1997.

[62] F. Ulaby, M. C. Dobson, and J. L. Álvarez-Pérez, *Handbook of Radar Scattering Statistics for Terrain*, Artech House, Norwood, MA, USA, 2019.

[63] J. P. Reilly, R. L. McDonald, and G. D. Dockery, "RF-Environment Models for the ADSAM Program," Report No. A1A97U 070, Johns Hopkins University Applied Physics Laboratory, Laurel, MD, USA, 1997. Available: https://apps.dtic.mil/sti/tr/pdf/ADA346190.pdf (accessed Feb. 3, 2024).

[64] M. W. Long, *Radar Reflectivity of Land and Sea*, 3rd ed., Artech House, 2001.

[65] MathWorks, "Reflectivity of Land Surface." Available: https://www.mathworks.com/help/radar/ref/landreflectivity.html (accessed Jan. 27, 2024).

[66] A. Abbas, M. Elsaid, S. F. Mahmoud, E. A. Abdallah, and H. M. El-Hennawy, "Link Budget Analysis for FMCW Radio Altimeter," in *Proc. 2021 Int. Telecommun. Conf. (ITC-Egypt)*, Alexandria, Egypt, Jul. 13–15, 2021, IEEE, pp. 1–4.

[67] MathWorks, "FMCW Radar Altimeter Simulation." Available: https://www.mathworks.com/help/radar/ug/fmcw-radaraltimeter-simulation.html (accessed Jan. 28, 2024).

[68] L. V. Blake, "A Guide to Basic Pulse-Radar Maximum-Range Calculation Part 1—Equations, Definitions, and Aids to Calculation," Naval Research Laboratory, Radar Geophysics Branch, Radar Division, Washington, DC, USA, 1969. Available: https://apps.dtic.mil/sti/pdfs/AD0701321.pdf (accessed Feb. 8, 2024).

[69] Honeywell, "ALA-52B Radio Altimeter." Available: https://aerospace.honeywell.com/us/en/products-and-services/product/hardware-and-systems/navigation-and-radios/ala-52b-radar-altimeter (accessed Jan. 22, 2024).

[70] D. D. Nguyen, J. Rohacs, and D. Rohacs, "Autonomous Flight Trajectory Control System for Drones in Smart City Traffic Management," *ISPRS Int. J. Geo-Inf.*, vol. 10, p. 338, 2021.

[71] C. E. Shannon, "Communication in the Presence of Noise," *Proc. IRE*, vol. 37, pp. 10–21, 1949.

[72] K. Ramasubramanian, "Using Complex-Baseband Architecture in FMCW Radar Systems." Available: https://www.ti.com/lit/pdf/spyy007 (accessed Jan. 23, 2024).

[73] C. A. Balanis, *Antenna Theory: Analysis and Design*, 4th ed., John Wiley & Sons, Inc., Hoboken, NJ, USA, 2015.

[74] MathWorks, "Radar Data Cube." Available: https://www.mathworks.com/help/phased/gs/radar-data-cube.html (accessed May 11, 2024).

[75] I. G. van de Zande, "3D Point Cloud Object Detection for Millimeter Wave Radar: A Synthesis Study," M.S. thesis, Univ. of Twente, Enschede, The Netherlands, Sep. 2023.

[76] S. Rao, J. Nayyar, M. Yan, and B. Johnson, "Introduction to the DSP Subsystem in the AWR16xx," Texas Instruments, Dallas, TX, USA, May 2017.

[77] Q. Chaudhari, "FMCW Radar Part 2—Velocity, Angle and Radar Data Cube." Available: https://wirelesspi.com/fmcwradar-part-2-velocity-angle-and-radar-data-cube/ (accessed Apr. 5, 2024).

[78] National Instruments, "Understanding FFTs and Windowing." Available: https://download.ni.com/evaluation/pxi/Understanding%20FFTs%20and%20Windowing.pdf (accessed May 12, 2024).

[79] A. V. Oppenheim and R. W. Schafer, *Discrete-Time Signal Processing*, 2nd ed., Prentice Hall, Upper Saddle River, NJ, USA, 1999.

[80] Skybrary, "Cruise." Available: https://skybrary.aero/cruise (accessed Mar. 17, 2024).

[81] National Oceanic and Atmospheric Administration, "Radar Images: Velocity." Available: https://www.noaa.gov/jetstream/velocity (accessed Jun. 2, 2024).

[82] MathWorks, "Reflectivity of Land Surface." Available: https://www.mathworks.com/help/radar/ref/landreflectivity.html (accessed Mar. 27, 2024).

[83] MathWorks, "Constant False Alarm Rate (CFAR) Detection." Available: https://www.mathworks.com/help/phased/ug/constant-false-alarm-rate-cfar-detection.html (accessed May 9, 2024).

[84] DJI, "Matrice 30 Series, Specifications." Available: https://enterprise.dji.com/matrice-30/specs (accessed May 11, 2024).

[85] U.S. Department of Transportation, Federal Aviation Administration, *Airplane Flying Handbook*, U.S. Department of Transportation, Federal Aviation Administration, Oklahoma City, OK, USA, 2021, ISBN 979-8776143243.

[86] MathWorks, "Normalized Sea Surface Reflectivity." Available: https://www.mathworks.com/help/radar/ref/seareflectivity.html (accessed May 12, 2024).

[87] A. Venon, Y. Dupuis, P. Vasseur, and P. Merriaux, "Millimeter Wave FMCW RADARs for Perception, Recognition and Localization in Automotive Applications: A Survey," *IEEE Trans. Intell. Veh.*, vol. 7, pp. 533–555, 2022.

[88] F. J. Abdu, Y. Zhang, M. Fu, Y. Li, and Z. Deng, "Application of Deep Learning on Millimeter-Wave Radar Signals: A Review," *Sensors*, vol. 21, p. 1951, 2021.

[89] A. N. Wilson, A. Kumar, A. Jha, and L. R. Cenkeramaddi, "Embedded Sensors, Communication Technologies, Computing Platforms and Machine Learning for UAVs: A Review," *IEEE Sens. J.*, vol. 22, pp. 1807–1826, 2022.

[90] J. Coonrod, "Reliably Bend and Form Microwave PCBs," *Microw. J.*, vol. 56, p. 92, 2013.

[91] Texas Instruments, "mmWave Demo Visualizer." Available: https://dev.ti.com/gallery/view/mmwave/mmWave_Demo_Visualizer/ver/4.4.0/ (accessed Feb. 8, 2024).

[92] "Hysteresis in Digital Control Systems." Available: https://www.hwe.design/theories-concepts/hysteresis (accessed Jun. 20, 2024).

[93] M. A. Awan, Y. Dalveren, A. Kara, and M. Derawi, "*Towards mmWave Altimetry for UAS: Exploring the Potential of 77 GHz Automotive Radars*," Drones, vol. 8, no. 3, p. 94, Mar. 2024.

[94] M. A. Awan, Y. Dalveren, A. Kara, and M. Derawi, "*Advancing mmWave Altimetry for Unmanned Aerial Systems: A Signal Processing Framework for Optimized Waveform Design*," Drones, vol. 8, no. 9, p. 440, Aug. 2024.